

# Ground-Truth based Performance Assessment of Landslide Susceptibility Mapping: A Case Study after Elazig Earthquake (24 Jan 2020, Mw 6.8), Turkey

Gizem Karakas

Hacettepe University: Hacettepe Universitesi

Sultan Kocaman (✉ [sultankocaman@hacettepe.edu.tr](mailto:sultankocaman@hacettepe.edu.tr))

Hacettepe University: Hacettepe Universitesi <https://orcid.org/0000-0002-2775-7914>

Candan Gokceoglu

Hacettepe University: Hacettepe Universitesi

---

## Research Article

**Keywords:** Landslide Susceptibility Mapping, Performance Assessment, Machine Learning, Photogrammetry, Multi-Layer Perceptron, Random Forest

**Posted Date:** August 26th, 2021

**DOI:** <https://doi.org/10.21203/rs.3.rs-825972/v1>

**License:**  This work is licensed under a Creative Commons Attribution 4.0 International License.  
[Read Full License](#)

---

# Abstract

Quality assessment for landslide susceptibility maps (LSMs) is essential to increase their usability. Ground-truth based quality assessment is crucial for performance evaluation of LSM production methods. Landslides triggered by earthquakes can be employed for this purpose as they occur frequently throughout the active seismic regions of the world. After an earthquake occurred in Elazig, Turkey on 24 Jan 2020 (Mw 6.8), several landslides were activated in the mountainous parts. Here, the performances of two state-of-the-art machine learning methods, i.e., random forest (RF) and multi-layer perceptron (MLP), were investigated using the activated landslides. The landslide inventory was derived by using pre- and post-event aerial photogrammetric datasets; whereas only the pre-event datasets were utilized for LSM production. The inventory includes activity classes of inactive (L1) and active mass movements (L2), areas having new active zones occurred after 2018 inside the existing landslide (L3), and new activity after 2018 (L4). The L1 and L2 type landslides were used in model training, while L3 and L4 type landslides triggered by the earthquake were used for validation. The area under curve (AUC) values and volumetric change maps obtained from the pre- and post-event datasets were also used for the performance assessment. Furthermore, only a part of the study area was used for model training while the LSMs were produced for the whole area. The results demonstrated that RF exhibited higher classification accuracy (AUC = 0.93) than MLP (AUC = 0.87); and accurate LSMs could be produced by using a sub-part of the basin for training.

## 1. Introduction

At times, landslides triggered by earthquakes cause more damages and losses of lives than the direct effects of the earthquake. However, often the damages caused by landslides triggered by earthquakes (Fan et al. 2018; Tsou et al. 2018; Zhao et al. 2019; Goorabi et al. 2020; Barth et al. 2020) are directly reported as earthquake damages; and consequently the records are distorted and the necessary attention is not paid. To explain this issue in numbers, 5%-11% of all deaths during earthquakes are caused by landslides triggered by earthquakes (Marano et al. 2009; Daniell et al. 2017). In other words, landslide events occurred with earthquakes in the period between 1968 and 2008 caused approximately 71,000 fatalities (Jesse et al. 2020). Jesse et al. (2020) have prepared a detailed inventory triggered by earthquakes covering a 207-year period from 1811 to 2016. Using this database, the models proposed by Jesse et al. (2020) can predict the deaths that will result from landslides triggered by earthquakes. This estimation will undoubtedly provide great benefits in terms of planning and efforts to reduce losses due to landslides triggered by earthquakes. However, the most fundamental necessity here is to determine the landslide areas that are likely to be triggered by landslides.

If a region is susceptible to landsliding, which is likely to be triggered by earthquakes, regional landslide susceptibility assessments become even more important in terms of reducing earthquake-related damages. Kumar et al. (2021) also emphasized that mapping the areas prone to coseismic landslides in seismically active regions is essential. The Newmark (Newmark 1965) and/or the infinite slope models have been widely used in the literature for regional landslide susceptibility assessments triggered by

earthquakes (Havenith et al. 2006; Das et al. 2013; Rodrigues-Peces et al. 2014; Chen et al. 2020a; Shinoda and Miyata 2017; Shinoda et al. 2019; Li and Su 2021; Nayek and Gade 2021). However, such models require accurate and representative geomechanical parameters of the slope forming materials. Although the geomechanical parameters of the material forming the slope can be used in the regional landslide assessments (Gokceoglu and Aksoy 1996), such a process is very difficult and cannot produce highly accurate results for complex geological environments. Therefore, conventional landslide susceptibility maps (LSMs) still pursue their importance. In the recent literature, it is possible to find studies on regional susceptibility assessments of landslides triggered by earthquakes (e.g. Xie et al. 2018; Chen et al. 2020 a, b, c; Chen et al. 2021). However, if there is no landslide inventory prepared immediately after earthquake, it is still difficult to distinguish the landslides in a region that are triggered by earthquakes. Therefore, LSM production efforts must consider coseismic landslide inventory of a region for analyzing the effects of seismic events and for improved landslide hazard assessment. Such inventories are also useful for the evaluation of the prediction performances of LSMs produced with novel machine learning (ML) methods.

On 24 January 2020, at 20:55, the Elazig earthquake of 6.8 magnitude with a duration of 20.4 s occurred. The area affected by the earthquake is located around the Eastern Anatolian Fault Zone (EAFZ). A large part of the region has mountainous topography, and is prone to landsliding. Thus, the Elazig earthquake triggered several landslides. Two landslide inventories of the region, one before the earthquake and the other one representing the landslides triggered by the earthquake were compiled by Karakas et al. (2021 a). In order to prepare an up-to-date LSM of the region, the conditioning factors, in particular the geological and geomorphological characteristics which control landslides, should be considered. Chen et al. (2012) described the large landslides triggered by the Wenchuan earthquake and concluded that large catastrophic landslides can be related to a particular geological setting, where fault type and geometry change abruptly. Consequently, if the completed event-based landslide inventory map is available, it is possible to produce an accurate LSM for the related event. Moreover, when fully complete pre- and post-event landslide inventory maps and digital surface models (DSMs) are available, it can be possible to assess the accuracy of the LSM and the performance of the method used for its production.

In the literature, several ML methods and statistical techniques have been proposed to evaluate the LSMs (e.g. Pradhan et al. 2010; Nefeslioglu et al. 2012; Wang et al. 2016; Dagdelenler et al. 2016; Sevgen et al. 2019; Karakas et al. 2020; Kocaman et al. 2020; Medina et al. 2021; Can et al. 2021; Bera et al. 2021; Qi et al. 2021). In recent years, a significant rise in LSMs produced by using data-driven ML methods has been observed. Algorithms such as artificial neural networks (ANNs), support vector machine (SVM), decision tree (DT), random forest (RF), gradient boosting machine (GBM), fuzzy logic (FL) and logistic regression (LR) are among the ML algorithms used to produce LSMs (e.g. see Pourghasemi et al. 2012; Wang et al. 2016; Sevgen et al. 2019; Karakas et al. 2020; Wang et al. 2020; Yanar et al. 2020; Qi et al. 2021; Wu et al. 2021). Wang et al. (2020) compared susceptibility results for landslide prediction using five methods such as LR (0.77), SVM (0.80), RF (0.82), GBM (0.81) and MLP (0.80) in Shexian County. Among the five algorithms, RF yielded the best accuracy results. Bui et al. (2020) compared the accuracy of a deep learning neural network model (DLNN) with state-of-the-art ML algorithms in landslide susceptibility

assessment and found that DLNN model obtained higher performance (0.90) followed by the multi-layer perceptron (MLP) (0.87). Adnan et al. (2020) proposed an approach for uncertainty reduction in landslide mapping that evaluated the compatibility of landslide prediction maps produced using four ML algorithms (k-nearest neighbors algorithm (k-NN), MLP, RF and SVM). The prediction results indicated that the RF model had the highest performance followed by the MLP, SVM, and k-NN models.

The supervised ML algorithms used for the LSMs mentioned above frequently utilized the receiver operating characteristics (ROC) including the area under the curve (AUC) value for the performance evaluation. However, these indicators are obtained from the existing landslide inventory (i.e. model training and test data) and this kind of quality assessment may be insufficient as the LSMs aims at predicting future landslide activities (Sevgen et al. 2019). Therefore, the purpose of the present study is to evaluate the performances of two different state-of-the-art ML methods, such as the RF and the MLP, for the LSM production in a mountainous region prone to landslides and with high seismicity by using the ground-truth information obtained from the new landslide activities (inventory) occurred after the earthquake together with the volumetric change maps of the study area. The statistical values (i.e. ROC curve and AUC) obtained from the methods were also assessed for controlling the model training. Besides producing the LSMs for the area, the three different approaches were used to validate the performances of the LSMs, which is the main novelty of the study. Furthermore, only a part of the landslide inventory located in the western part of the study area was used for the model training and the LSMs were produced for the whole study area.

The area is located in the Malatya and Elazig Provinces of Turkey. For the purpose of the study, the landslide inventories with time tags (i.e., before and after the Elazig earthquake) derived by Karakas et al. (2021 a) were employed. Aerial photogrammetric datasets acquired in pre-event and post-event dates were utilized for the preparation of the landslide inventory and to detect the 3D changes from the produced high-resolution DSMs. The data obtained by photogrammetric methods were used in the ML models to produce the LSMs. The pre-earthquake datasets were acquired in two different years (2017 and 2018) during regular photogrammetric mapping campaigns of General Directorate of Mapping (GDM), Turkey. The temporal difference was caused by the flight planning based on province boundaries (2017 for Malatya and 2018 for Elazig Provinces). Therefore, the ML methods were trained only by using the data that remains in Malatya Province located in the western part of the study area; and the LSMs were produced for both provinces using the same model parameters. Thus, transferability of the model parameters to the different parts of the same geographical area was also assessed in the study. The preliminary LSM results of the area were obtained with the RF method by using the inventory of both parts for model training (Karakas et al. 2021 b) and the AUC results of the test pixels were 0.90 and 0.92 in Malatya and Elazig parts, respectively. A frequency ratio analysis between the landslide occurrence and the pre-defined conditioning factors was also presented by Karakas et al. (2021 b).

## 2. Material And Methods

### 2.1 Study Area Characteristics

The study area is located in the south eastern part of Turkey in the administrative boundaries of Malatya and Elazig Provinces (Figure 1). As there is high seismicity and active tectonism in the region, the topography is very young and steep. Therefore, the lithological units have weak shear strength characteristics. Due to the topographical and lithological characteristics, the area is prone to landsliding (Sevgen et al. 2019). The frequency ratio analysis presented by Karakas et al. (2021 b) indicated that Maden Complex, Puturge Metamorphites and Unconsolidated Gravel, Sand, Silt, Clay lithological units are most prone for landslides. The Puturge Metamorphites of uncertain age (Paleozoic to Mesozoic) in the study area is composed of different metamorphic rock units (gneiss, aphyllite, calc-schist etc.) of different origin, whereas pebblestone, sandstone, limestone, spilitic basalt etc constitute the lithology of the Maden Complex of early to middle Eocene age (Keskin 2002). The geological characteristics of the study area is provided in Figure 2. The geological units vary with the altitudes, such as magmatic and metamorphic rocks exist in the upper altitudes whereas young sedimentary rock are observed in the lower altitudes. Figure 1 depicts also the produced DSMs of the study area obtained from two different photogrammetric flight missions carried out in 2017 and 2018 in Malatya and Elazig Provinces, respectively. Thus, the datasets were named after Malatya and Elazig for clarity and processed separately for these two parts. The maps in Figures 1 and 2 are presented in Universal Transverse Mercator (UTM) projection and World Geodetic System 1984 (WGS84) Datum Zone 37 North with the unit of meters (European Petroleum Survey Group – EPSG code 32637). While the altitude values range between 453 m and 2172 m for the Malatya part in the study area, they range between 553 m and 2031 m for the Elazig part. The frequency ratio results presented by Karakas et al. (2021 b) have shown that approximately 1000 m – 1650 m altitudes are more critical for landslide occurrence. After the Elazig Earthquake, several slope deformations and failures were observed and reported by several researchers (Tatar et al. 2020; Gokceoglu et al. 2020; Cetin et al. 2021; Temur et al. 2021).

## ***2.2 Photogrammetric Datasets***

The aerial photos were processed in three sets based on the dates of the acquisitions. The first two sets were acquired in 2017 and 2018 over Malatya and Elazig, respectively. The last set was acquired on 26 Jan 2020, two days after the earthquake event and used for the validation of the results. The datasets were obtained from the GDM together with image exterior orientation and camera calibration parameters. The pre-event datasets, which were used for the LSM production, were composed of a total of 142 aerial photos. All images were taken with 80% forward and 60% lateral overlap using UltraCam Eagle 1 large format digital aerial camera. These aerial photos have 30 cm spatial resolution and were processed to produce high resolution DSMs with 5 m grid spacing and orthophotos with 2 m spatial resolution. Since the exterior orientation parameters were provided in UTM 37N (EPSG: 32637) projection system, the DSMs and orthophotos were produced in this system and all maps derived from them have the same coordinate reference system (CRS) definition. The post-event dataset was acquired for the earthquake region for disaster mitigation purposes by the GDM and has 20 cm resolution. The dataset contains 1410 aerial images. The photogrammetric dataset was explained more detail in a previous publication (Karakas et al. 2021 a).

## **2.3 The Earthquake Event and the Landslide Inventory**

The Elazig earthquake with the Mw of 6.8 occurred on the Hazar-Sincik Segment of the EAFZ on January 24, 2020 (AFAD 2020). The maximum acceleration was measured as 0.293 g by Turkey Disaster and Emergency Management Presidency (AFAD). The landslide inventory data were delineated manually using visual interpretations the orthophotos and the DSMs (Gokceoglu et al. 2020; Karakas et al. 2021 a). The smallest and the largest landslide areas are  $133 \text{ m}^2$  and  $3 \times 10^6 \text{ m}^2$ , respectively. The landslide activities were classified into four groups, such as (i) inactive mass movements (L1), (ii) active mass movements (L2), (iii) areas containing new active zones occurred after 2018 inside the existing landslide (L3), and (iv) newly developed areas after 2018 (L4), thus triggered by the earthquake. Out of a total of 328 landslides mapped by Karakas et al. (2021 a), 316 of them were utilized in the present study (Figure 3). In addition, an iso-intensity map of the earthquake event was prepared by Yalcin et al. (2020a) using citizen science methods as proposed by Yalcin et al. (2020 b) (Figure 4). The distribution of the landslides are provided in Figure 4. As can be seen from the Figure, the study area and the landslides are located in areas with intensity values between 5-7.

## **2.4 Methodology**

The overall methodological workflow is provided in Figure 5. Aerial photogrammetric datasets from 2017, 2018 and 2020 were used to produce the high resolution DSMs and orthophotos. The topographic derivatives of the study area, such as slope, aspect, plan and profile curvature, etc., were computed from the DSMs of the pre-event acquisitions (i.e. 2017 and 2018). The lithology data were digitized from 1:100,000 scale geological maps (Akbas et al. 2016), and rasterized with 5-m grid spacing. The landslide inventory and the features extracted from the topographic data were used to produce the LSMs by employing the RF and MLP methods. The LSMs were validated using the test (validation) data, which were not utilized in the model training and were also compared with the landslide inventory which was not included in the training. L1 and L2 type landslides, which fall into the Elazig part of the study area were excluded from the training. The L3 and L4 type landslides triggered by the event were omitted from the LSM prediction and used for validation purposes only. In addition, the volumetric change detection maps produced in a previous study (Karakas et al. 2021 a) were used for visual inspection.

### **2.4.1 Feature Extraction for Landslide Susceptibility Mapping**

Chang et al. (2021) investigated the coseismic landslides triggered by the 2018 Iburi Earthquake and the described key factors on the landslides triggered by the Iburi Earthquake are peak ground acceleration (PGA), lithology, distance to fault, distance to river, altitude, slope, aspect and curvature. Similarly, Mahalingama and Kim (2021) studied the effects of conditioning and triggering factors (such as slope, slope roughness, aspect, land use land cover (LULC), mean annual precipitation, distance to roads, rivers, PGA, and epicenters of the main shock earthquake and aftershocks) of landslides triggered by the Nepal

Earthquake. When preparing susceptibility map of landslides triggered by earthquakes, Wang et al. (2021) employed elevation, aspect, slope angle, terrain relief, distance to faults, distance to rivers and terrain wetness index as conditioning factors while Li et al. (2021) considered elevation, slope, aspect, land cover, soil type, precipitation, distance to faults, distance to roads and distance to streams for investigating earthquakes on landslides susceptibility in a seismic prone area in Central Asia. Several studies (Chen et al. 2021; Guo et al. 2021; Liu et al. 2021) considered similar conditioning and triggering parameters when producing susceptibility maps of landslides triggered by earthquakes. Consequently, different conditioning factors such as altitude, slope, aspect, plan and profile curvature, lithology, topographic wetness index (TWI), stream power index (SPI), normalized difference vegetation index (NDVI), drainage density, distance to roads were used to produce LSM in the literature (Chen et al. 2017b; de Oliveira et al. 2019; Wang et al. 2020; Adnan et al. 2020; Bui et al. 2020).

The conditioning factors used for the landslide susceptibility modeling in the study can be investigated in two sub-categories, such as topographical and geological. The PGA or another earthquake-related parameter was not considered here because it is the main trigger of the landslides inventoried in the study. Consequently, the PGA should be used in landslide hazard assessment. The topographic factors considered here include seven parameters, such as altitude, slope, aspect, TWI, SPI, and plan and profile curvatures as summarized previously. The geodata types with their resolution/scale used in the study are shown in Table 1. These parameters were derived from the DSMs of 2017 and 2018. As an additional feature, the lithology data obtained from Akbas et al. (2016) were included in the prediction. The lithology is one of the parameters defining the most important unit in which the landslide occurred. These parameters are frequently used for producing the LSMs in the literature (e.g. see Gokceoglu and Ercanoglu 2001; Brenning, 2005; Nefeslioglu et al. 2012; Pourghasemi et al. 2013; Sevgen et al. 2019).

The slope represents the variation in elevations (Wilson and Gallant 2000). Aspect shows the steepest descent direction calculated in degrees clockwise from the North (Wilson and Gallant, 2000). The curvature is the change rate of slope gradient and aspect in a given direction. The two types of curvatures, which are mostly considered, are the plan and profile curvatures. They are the second derivatives of the digital elevation models (DEMs). The SPI defines the erosive power of flowing water (Zakerinejad and Maerker 2015). When calculating the SPI, the slope and the contributing area are used as shown in Equation 1 (Moore et al. 1991).

$$SPI = A_s \times \tan\beta \quad \text{Eq. 1}$$

where  $A_s$  is the catchment area and  $\beta$  is the slope gradient ( $^{\circ}$ ).

The TWI is used in the determination of the hydrological conditions of the topography; and refers to the location and dimensions of the water-saturated areas in the basin area. This approach was first proposed by Beven and Kirkby (1979). Moore et al. (1991) suggested Equation 2 to calculate the TWI.

$$TWI = \ln\left(\frac{A_s}{\tan\beta}\right) \quad \text{Eq. 2}$$

where  $A_s$  is the catchment area and  $\beta$  is the slope.

## 2.4.2 Landslide Susceptibility Mapping with MLP and RF

In this study, the RF and MLP methods were applied for LSM production and their performances were compared by using different approaches to produce the landslide susceptibility of the study area. The models are data-driven and learns the probability of spatial occurrence of the landslides from the data, i.e. by using landslide and non-landslide samples given for the area. The input features explained previously were used as conditioning factors for the prediction.

ANNs are nonlinear statistical data models that are inspired from biological neural networks (NNs) (Jain et al. 1996). The MLP is a feedforward NN (Abiodun et al. 2019) and is currently a popular and widely used a supervised learning algorithm. It consists of two layers as input and output, and one or more hidden layers between them (Figure 6). Each neuron in the hidden layer processes the values from the previous layer with a weighted linear summation. The output layer receives the values from the last hidden layer and produces the output values (Chen et al. 2017a; Zare et al. 2013; Harmouzi et al. 2019; Sahana et al. 2020). In this study, the method was implemented using the Scikit-learn library (Scikit-learn 2021) in Python programming environment. The final transformation was performed by using a non-linear activation function. The formula for MLP is given in Equation 3.

$$x_n^m = f(\sum_{k=0}^i w_k^m x_k^{m-1}) \quad \text{Eq. 3}$$

where  $f$  represents the activation function,  $i$  is the number of neurons in layer  $m$ ,  $w_k^m$  refers the weight of  $k^{\text{th}}$  neuron in layer  $m$ ,  $x_k^{m-1}$  is the activation of  $k^{\text{th}}$  neuron in layer  $m-1$ ,  $n$  is the neuron indices, and  $j$  is the layer indices.

As shown in Figure 6, the input layer is composed of a set of neurons representing the input features (altitude, slope, aspect etc.). Here, the input layer has eight neurons containing the conditioning factors. The network was modelled with one hidden layer with 100 neurons in each. The Relu activation function was applied for the hidden layer. The Adam algorithm was used for weight optimization across the nodes. This algorithm is a stochastic gradient-based optimizer proposed by Kingma and Ba (2014). The maximum iteration denotes the number of epochs and used as 150 here. The learning rate approach used for weight updates was adaptive.

The RF algorithm is a powerful ensemble learning method of decision trees (DTs) (Breiman 2001). This algorithm creates DTs by a random selection at the training stage. The DTs are evaluated for the best score based on the average of the results of the trees. The most important features are in principle selected from all trees for classification. The RF minimizes the correlation between trees and provides higher classification performance. The general expression of RF is given in Equation 4. The number of trees in RF defines how many DTs will be created while the model is being trained. Another

important parameter is the maximum depth of the tree. In the present study, the hyperparameters used for running the RF and MLP algorithms were chosen heuristically. Since successful results were obtained by using these parameters in previous studies using aerial photographs, similar parameters were also used in this study (Sevgen et al. 2019; Karakas et al. 2020). The parameters used for each algorithm are summarized in Table 2.

$$Y(x) = \arg_{\mathbf{z}}^{\max} \sum_{n=1}^k I(y_n(x) = Z) \quad \text{Eq. 4}$$

where  $Y(X)$  represents RF model,  $\mathbf{z}$  represents a single decision tree model,  $Z$  is the output variable and  $I(\cdot)$  denotes the indicative function.

The RF and MLP algorithms were performed using Python scikit-learn library (Scikit-learn, 2021). Only the landslides with activity type 1 and 2 were used to train the model. These landslides were denoted by black (L1) and blue (L2) areas in Figure 7. Due to the imbalanced distribution of the landslide inventory in the study area, a sub-area of Malatya part (marked with red rectangle in Figure 7) was used for the model training for landslide and non-landslide samples. The ratio of the landslide non-landslide samples was 1:2 as performed by Yanar et al. (2020). The other landslides, which fall outside the red rectangle in Figure 7, were not employed during the model training stage but utilized for the performance assessment. The trained model was used for the LSM production for the whole study area including Malatya and Elazig parts. A training/test ratio of 70/30 percent of all samples were used for the model training and testing. Finally, the natural breaks classification was used to reclassify the predicted values into five categories using the Jenks optimization algorithm (Jenks 1967) implemented in ArcGIS software from ESRI Inc. USA. The algorithm minimizes the squared deviations of the class means and has the potential for an improved representation of the spatial distribution pattern in the data.

### **2.4.3 Accuracy Assessment and Validation**

Three performance assessment approaches were employed in this study. The first one was the assessment of the prediction performance metrics obtained from the ROC curve, including the AUC; and the visual analysis of the ROC curve. The second assessment approach was the comparison of the prediction results with the landslide inventory, in particular the L3 and L4 types, which occurred after the acquisition dates of aerial photogrammetric data (i.e. 2017 and 2018) used for the LSM production. Thus, it is expected that the L3 and L4 type landslides must be located in highly susceptible areas.

As the last approach, the performances of LSMs for both parts were assessed by visual comparison with the volumetric change maps with the same expectation (i.e. the L3 and L4 type landslides can be observed in the changes). Here, it must be noted that the surface changes were not only sourced from the earthquake-induced mass movements; but also include seasonal and land use land cover (e.g. vegetation, infrastructure, buildings, snow cover, etc.) changes in the area in the period of 2-3 years

(Karakas et al. 2021 a). The LS3D (least square surface matching) software developed by Gruen and Akca (2005) was used for the production of volumetric change maps.

## 3. Results

### 3.1 Topographic Derivatives

The statistical values obtained from the altitude values and the derived topographic features, which include slope, aspect, plan and profile curvatures, TWI, and SPI are provided separately for Malatya and Elazig DSMs in Tables 3 and 4. The statistical summary explains the minimum (Min), Maximum (Max), Mean, Standard Deviation (s), and the Median (Med) values for the whole area (Table 3) and the parts inside the landslide inventory (Table 4). The slope values range from 0° to 87° for the study area and the majority of the slopes accumulates between 20-25° degrees. The higher slope values were observed along directions of northeast-southwest (NE-SW) and northwest-southeast (NW-SE). The spatial distributions (maps) are provided in Figures 8, 9, 10, 11, 12 and 13. When the aspect map is analyzed (Figure 9), no accumulation in the values was observed.

The histograms of all topographic parameters are presented in Figures 14 and 15 for the Malatya and Elazig parts, respectively. The peaks in the altitude histograms are caused by the erroneous altitude values over the water surface. These errors are sourced from the false image matches in the DSM production process due to the textureless surface. The distributions of the plan and profile curvatures, TWI and SPI are in Gaussian pattern.

### 3.2 Ground-truth based Quality Assessment and Validation Results

#### 3.2.1 Prediction Results

Figure 16 shows the ROC curves and the AUC values obtained from the RF model (Figure 16a) and the MLP model (Figure 16b). A total of 350,412 landslide and 700,824 non-landslide pixel samples were used for the training (735,865 pixels) and testing (315,371 pixels). The total number of samples contained in the eight feature sets was 8,409,888. In Figure 16, the classes 0.0 and 1.0 reflect the non-landslide and landslide pixels. The curves were obtained from the training and test samples obtained from the training area, which is depicted with red rectangle in Figure 7. A ratio of 70/30 was preferred between the training and test samples. The AUC values were for both the non-landslide and landslide classes are 0.93 for the RF model. For MLP, these values were 0.87. These results show that the RF method exhibits higher prediction performance.

The produced LSMs are provided for Malatya and Elazig parts in Figure 17a (RF) and 17b (MLP). The LSMs were evaluated in five classes as very low, low, moderate, high and very high (Figure 17, Table 5)

obtained from the Jenks classification algorithm. The probability of occurrences are mostly at higher altitudes, but the slopes close to the water body and the drainage channels are also highly susceptible. Although the LSMs obtained from the both methods have similar patterns, the MLP has in general predicted lower susceptibility values in comparison to the RF especially for high and very high susceptibility areas.

Table 5 shows the areal distributions and the percentages of the different susceptibility classes in the predictions. The areas with high and very high susceptibility values obtained from the RF within Malatya part was  $36.94 \text{ km}^2$  and  $39.87 \text{ km}^2$ , respectively. The same classes in the Elazig part have coverages of  $32.51 \text{ km}^2$  and  $31.65 \text{ km}^2$ , respectively. When the areal coverages of high and very-high susceptibility classes obtained from the MLP method for Malatya (high:  $35.44 \text{ km}^2$ , very high:  $27.63 \text{ km}^2$ ) and Elazig (high:  $26.54 \text{ km}^2$ , very-high:  $33.57 \text{ km}^2$ ) are considered; the RF results show higher susceptibility values especially for Malatya part, even though the ranges obtained from Jenks classification are also higher for the RF. In Elazig part, MLP produced slightly more pixels in very-high susceptibility class, and less pixels in high susceptibility class in comparison to the RF.

### ***3.2.2 Comparison with Ground-truth Data from the New Landslides Inventory after the Earthquake***

A visual comparison between the landslide inventory and the predictions were carried out using Figure 18, which shows the LSMs and the inventory data in 3D perspective view. The pixels within the L3 (denoted with green) and L4 (denoted with pink) activity type landslides were not considered in the model training stage. For Malatya Part RF results, when the probability of the susceptibility results in the produced LSM was considered, the probability values between 0.55 and 0.76 indicate high class, and probability values between 0.76 and 1.00 correspond to very high class. For the Elazig Part RF results, these values are between 0.59 and 0.79 in the high class and between 0.79 and 1.00 in the very high class (Figure 17a). When the MLP results are analyzed in Figure 17b for Malatya Part, the probability values are between 0.53-0.75 in the high class and 0.75-1.00 in the very high class. For Elazig Part, the values are between 0.55 and 0.79 in the high class and between 0.79 and 1.00 in the very high class. In addition, a statistical summary of the susceptibility predictions obtained from a total of 69 L3 and L4 type landslides are provided in Table 6 for both methods. The values were grouped per region and the landslide types. According to the Table, the RF method predicted higher susceptibility values both for Elazig (mean values for L3: 0.62 and L4: 0.74) and for Malatya (mean values for L3: 0.64 and L4: 0.53) in comparison to the MLP. This shows transferability of model parameters for RF for similar sites. These values show the success of RF and MLP models. On the other hand, according to Figure 18, the MLP results seem to be a better fit when different geological characteristics are observed between the training and validation sites. As can be seen in Figure 2, the lithological unit of unconsolidated gravel, sand, slit, clay type exists more in Elazig part and less in Malatya. The area is marked with red dashed ellipses in the Figure 18. Thus, the MLP produced more successful results in this lithological unit in Elazig.

### **3.2.3 Volumetric Change Detection Results**

The volumetric change detection was performed previously by Karakas et al. (2021 a) using high-resolution DSMs produced from pre- and post-earthquake aerial photos. The Euclidean distances (i.e. discrepancies) between the DSMs were calculated using the LS3D software. Figure 19 shows the Euclidean distance residual plots of Malatya and Elazig parts together with the landslide inventory. The red and the blue colours in Figure 19 demonstrate the largest elevation changes in meters. The results were assessed visually. Figures 20, 21 and 22 show sub-areas from the different parts with their change detection maps, RF and MLP LSMs, and orthophotos from the pre- and post-event datasets. Note that the L3 activity type landslides are depicted with red polygons instead of green for increasing their visibility on the change detection maps.

## **4. Discussion**

The present study provided a comparative evaluation of various validation approaches for the LSMs, which were produced using two different supervised ML classifiers, i.e. the RF and the MLP methods. The classifications were performed for pixels. The landslide inventory produced by Karakas et al. (2021 a) is a comprehensive one reflecting the landslides triggered by the Elazig Earthquake (24 Jan 2020, Mw 6.8) occurred in Turkey. Considering the activity type, the landslide inventory was classified into four categories, such as inactive (L1), active (L2), areas containing new active zones occurred after 2018 inside the existing landslide (L3), and newly developed areas after 2018 (L4), thus triggered by the earthquake. The LSMs were produced using the pre-event DSMs and the topographic derivatives, the geological characteristics of the area (lithology), and only the two types of landslides (L1 and L2), which were observable in the site in the pre-event datasets and thus were not triggered by the earthquake. The results were validated using the ground-truth, i.e. the L3 and L4 activity type landslides. The LSMs were produced separately for the two sub-parts of the study area, i.e. Malatya and Elazig parts, due to approximately one year difference between the acquisitions of photogrammetric datasets in these provinces. There were a total of 40 landslides with activity type L3 and L4 for the Malatya part of the study area, and 29 landslides in total for the Elazig part.

The outcomes of the study can be discussed as follows;

- The conditioning factors derived in the present study are the factors commonly used in the literature (e.g. see Gokceoglu and Ercanoglu 2001; Brenning 2005; Nefeslioglu et al. 2012; Pourghasemi et al. 2013; Sevgen et al. 2019; Chang et al. 2021; Guo et al. 2021; Mahalingama and Kim 2021). These parameters were found to be sufficient for obtaining high performance in landslide susceptibility modeling here. Although it is possible to employ further parameters, highly correlated conditioning factors may cause multicollinearity problem.
- There are different supervised ML algorithms used for LSM in the literature. However, RF and MLP algorithms are the most commonly used and also accurate ones among these algorithms (Zare et al.

2013; Chen et al. 2017 a; Chen et al. 2017 b; de Oliveira et al. 2019; Harmouzi et al. 2019; Sevgen et al. 2019; Adnan et al. 2020; Karakas et al. 2020; Sahana et al. 2020). For this reason, in the study, RF and MLP algorithms were used to produce more accurate and effective LSM.

- The most important contribution of the study is the detailed comparison of three different approaches for validating the LSMs. The first approach was based on the ROC curve and AUCs obtained from the model outputs. The training/test ratio was 70/30 percent in the training area, which only falls inside Malatya part. The second approach was qualitative and quantitative validations via visual assessments on the LSMs and the L3 & L4 type landslides; and the analysis of prediction statistics for the pixels which fall into these landslides. The last approach was a qualitative evaluation based on the comparison of volumetric change maps and the LSMs.
- When the first approach is considered, the RF provides higher prediction performance with an AUC value equal 0.93 in comparison to the MLP (AUC = 0.87). The success of DTs and in particular the RF method for LSM production is well-known in the literature (e.g. see Chen et al. 2017 b; Sevgen et al. 2019; Adnan et al. 2020; de Oliveira et al. 2019; Karakas et al. 2020). In this study, the RF algorithm has proven to be successful.
- When the second approach is considered, the quantitative results presented in Table 6 show that the RF could predict higher susceptibility values for the L3 and L4 type landslide pixels with the mean values that fall into high susceptibility class as explained in Figure 17 and Table 5. For Malatya part, the MLP provided mean susceptibility values for both landslide types that remain in the moderately susceptible class. For Elazig part, the mean susceptibility value (0.56) inside the L3 type landslides fall into the high susceptibility class, whereas for L4 type the mean value was 0.53 and thus moderately susceptible. The standard deviations obtained from both methods are quite similar for both parts and range from 0.11 to 0.14. The median values are comparable to the mean values, which imply a normal distribution of the predictions. It must be noted here that the numbers and the sizes of L3 and L4 type landslides are diverse; and the L4 type landslides are smaller and less frequent.
- On the other hand, although the quantitative assessment in the second approach indicates the better performance of the RF, MLP was found more successful in a lithological unit which was not included in the model training area, which falls into the Malatya part. As can be seen from the Figure 22, MLP outperformed RF for this unit. Thus, it can be said that although the model parameters can be transferred to another site in the same basin, the RF is more sensitive to the changes in the data and may not be able to predict correctly.
- When the third approach is considered, a relationship between the residual maps and the LSMs can be observed. It can be thought that small movements inside the susceptible areas could be detected by the high resolution change detection map. Again, due to the DSM production approach and the temporal difference between the pre- and post-earthquake datasets, the Euclidian residuals presented here have uncertainties caused by the other types of surface changes.

- When the prediction performance obtained in the present study is compared to the results of Wang et al. (2020), it is seen that the AUC values obtained in the present study are higher than the other study (0.82 and 0.80 for RF and MLP). While the MLP results are similar with the study by Bui et al. (2020), RF (0.83) results are lower than that of this study. The main reason for this situation can be considered as data quality.
- When the landslide conditioning parameters applied here are considered, they are found sufficient. Although the LULC was not considered as an effective factor in the study, the LSMs can be updated when important LULC changes occur in the region. In addition, the new landslides triggered by the earthquake must be taken into account when the new LSM using the DSM of 2020 is produced.

## 5. Conclusions And Future Work

The study area is a region with high seismicity, which is located along the EAFZ. In addition, the study area is prone to landsliding. In this study, two LSMs were produced considering the data before the earthquake and their performances were assessed using the ground-truth based data after Elazığ Earthquake (24 Jan 2020, Mw 6.8). The RF and MLP algorithms were applied to produce the LSMs. The landslide inventory prepared by using pre-event datasets were used in the LSM production and validated against the landslides triggered by the earthquake together with the ROC curves and volumetric change detection map. Considering the AUC values, the RF outperforms the MLP. When the susceptibility values inside the landslides triggered by the earthquake were statistically analysed, again the RF provided higher values, which fall into high susceptibility class. On the other hand, in a lithological unit, which was not used for training, the MLP provided better performance. The results show that the RF can provide higher performance in different sites only if the similarity between the sites are also high. It is also recommended to check the LSMs via visual qualitative assessment.

The study contains two main novelties. One of these is the production of a susceptibility map with a landslide inventory map prepared before a major earthquake, and performance validation using the inventory map prepared after the earthquake. In particular, the existence of a landslide inventory both before and after the earthquake made a significant contribution to the performance evaluation. This contribution is another important novelty of the study. As a result, a procedure for assessing landslide susceptibility triggered by earthquakes was put forward by including these novelties in the study. After this stage, the production of landslide hazard maps and risk management will become more applicable, taking into account earthquake parameters as the triggers.

As a future recommendation, depending on the development of geo-spatial technologies, high resolution images to be obtained immediately after major earthquakes allow the inventory of triggered landslides to be compiled with high precision. Such inventories will enable the production of LSMs with much higher prediction capacity.

## Declarations

# Funding

No external funding was received for the study.

## Conflicts of Interest

The authors declare that there is no conflict of interest.

## Data Availability Statement

Data subject to third party restrictions. The aerial photogrammetric datasets were provided by the General Directorate of Mapping, Turkey, for research purposes and without the sharing permission publicly.

## References

Abiodun OI, Jantan A, Omolara AE, Dada KV, Umar AM, Linus OU, Arshad H, Kazaure AA, GanaU, Kiru MU (2019) Comprehensive review of artificial neural network applications to pattern recognition. IEEE Access, 7, pp.158820-158846. DOI: 10.1109/ACCESS.2019.2945545

Adnan MSG, Rahman MS, Ahmed N, Ahmed B, Rabbi MF, Rahman RM (2020) Improving Spatial Agreement in Machine Learning-Based Landslide Susceptibility Mapping. Remote Sens. 12, 3347. <https://doi.org/10.3390/rs12203347>

AFAD (Disaster and Emergency Management Presidency of Turkey) 2020. Report on the 24 January 2020 Sivrice (Elazig) Earthquake. 47p, <https://deprem.afad.gov.tr/downloadDocument?id=1831>.

Akbaş B, Akdeniz N, Aksay A, Altun İ, Balcı V, Bilginer E, Bilgiç T, Duru M, Ercan T, Gedik I, et. al. (2016) Turkey Geological Map Mineral Research & Exploration General Directorate Publication. Ankara, Turkey.

Barth S, Geertsema M, Bevington AR, Bird AL, Clague JJ, Millard T, Bobrowsky PT, Hasler A, Liu H (2020) Landslide response to the 27 October 2012 earthquake (MW 7.8), southern Haida Gwaii, British Columbia, Canada. Landslides, 17, 517–526. <https://doi.org/10.1007/s10346-019-01292-7>.

Bera S, Upadhyay VK, Guru B, Oommen T (2021) Landslide inventory and susceptibility models considering the landslide typology using deep learning: Himalayas, India. Nat Hazards, <https://doi.org/10.1007/s11069-021-04731-8>.

Beven KJ, Kirkby MJ (1979) A Physically Based, Variable Contributing Area Model of Basin Hydrology Hydrological Sciences Bulletin. Vol. 24, No. 1, p 43- 69.

Breiman L (2001) Random Forests. Machine Learning, 45, 5–32.

Brenning A (2005) Spatial prediction models for landslide hazards: review, comparison and evaluation. *Nat. Hazards Earth Syst. Sci.* 5, 853–862.

Bui DT, Tsangaratos P, Nguyen VT, Van Liem N, Trinh PT (2020) Comparing the Prediction Performance of a Deep Learning Neural Network Model with Conventional Machine Learning Models in Landslide Susceptibility. *Catena*, 188. <https://doi.org/10.1016/j.catena.2019.104426>

Can R, Kocaman S, Gokceoglu C (2021) A Comprehensive Assessment of XGBoost Algorithm for Landslide Susceptibility Mapping in the Upper Basin of Ataturk Dam, Turkey. *Appl Sci*, 11, 4993. <https://doi.org/10.3390/app11114993>.

Cetin KO, Cakir E, Ilgac M, Can G, Soylemez, B, Elsaad A, Cuceoglu F, Gulerce Z, Askan A, Aydin S, Gor M (2021) Geotechnical aspects of reconnaissance findings after 2020 January 24th, M6.8 Sivrice–Elazig–Turkey earthquake. *Bull Earthquake Eng*, <https://doi.org/10.1007/s10518-021-01112-1>.

Chang M, Zhou Y, Zhou C, Hales TC (2021) Coseismic landslides induced by the 2018 Mw 6.6 Iburi, Japan, Earthquake: spatial distribution, key factors weight, and susceptibility regionalization. *Landslides*, 18, 755-772, <https://doi.org/10.1007/s10346-020-01522-3>.

Chen XL, Ran HL, Yang WT (2012) Evaluation of factors controlling large earthquake-induced landslides by the Wenchuan earthquake. *Nat. Hazards Earth Syst. Sci.* 12, 3645–3657, doi:10.5194/nhess-12-3645-2012

Chen W, Pourghasemi HR, Zhao Z (2017 a) A GIS-based comparative study of Dempster-Shafer, logistic regression and artificial neural network models for landslide susceptibility mapping. *Geocarto international*. 32(4): 367-385., DOI: 10.1080/10106049.2016.1140824

Chen W, Xie X, Wang J, Pradhan B, Hong H, Bui DT, Duan, Z, Ma J (2017 b) A comparative study of logistic model tree, random forest, and classification and regression tree models for spatial prediction of landslide susceptibility. *Catena*. 151, 147-160. <https://doi.org/10.1016/j.catena.2016.11.032>.

Chen XL, Shan XJ, Wang MM, Liu CG, Han NN (2020 a) Distribution pattern of coseismic landslides triggered by the 2017 Jiuzhaigou Ms 7.0 earthquake of China: control of seismic landslide susceptibility. *ISPRS International Journal of Geo-Information*. 9(4): 198. <https://doi.org/10.3390/ijgi9040198>

Chen S, Miao Z, Wu L, He Y (2020 b) Application of an Incomplete Landslide Inventory and One Class Classifier to Earthquake-Induced Landslide Susceptibility Mapping. *IEEE Journal of Selected Topics in Applied Earth Observations and Remote Sensing*. 13, 1649-1660. DOI: 10.1109/JSTARS.2020.2985088

Chen L, Mei L, Zeng B, Yin K, Shrestha DP, Du J (2020 c) Failure probability assessment of landslides triggered by earthquakes and rainfall: a case study in Yadong County, Tibet, China. *Scientific reports*. 10(1):1-12. <https://doi.org/10.1038/s41598-020-73727-4>

Chen S, Miao Z, Wu L, Zhang A, Li Q, He Y (2021) A One-Class-Classifier-Based Negative Data Generation Method for Rapid Earthquake-Induced Landslide Susceptibility Mapping. *Front Earth Sci*, 9, 609896. <https://doi.org/10.3389/feart.2021.609896>.

Dagdelenler G, Nefeslioglu HA, Gokceoglu C (2016). Modification of seed cell sampling strategy for landslide susceptibility mapping: an application from the Eastern part of the Gallipoli Peninsula (Canakkale, Turkey). *Bulletin of Engineering Geology and the Environment*, 75 (2): 575-590. DOI: 10.1007/s10064-015-0759-0

Daniell JE, Schaefer AM, Wenzel F (2017) Losses associated with secondary effects in earthquakes. *Front Built Environ*, 3. <https://doi.org/10.3389/fbuil.2017.00030>.

Das HO, Sonmez H, Gokceoglu C, Nefeslioglu HA (2013) Influence of seismic acceleration on landslide susceptibility maps: a case study from NE Turkey (the Kelkit Valley). *Landslides*. 10: 433–454. <https://doi.org/10.1007/s10346-012-0342-8>

de Oliveira GG, Ruiz LFC, Guasselli LA, Haetinger C (2019) Random forest and artificial neural networks in landslide susceptibility modeling: a case study of the Fão River Basin, Southern Brazil. *Nat Hazard.s* 99, 1049–1073 <https://doi.org/10.1007/s11069-019-03795-x>

Fan X, Scaringi G, Xu Q, Zhan W, Dai L, Li Y, Pei X, Yang Q, Huang R (2018) Coseismic landslides triggered by the 8th August 2017 Ms 7.0 Jiuzhaigou earthquake (Sichuan, China): factors controlling their spatial distribution and implications for the seismogenic blind fault identification. *Landslides*, 15, 967–983. <https://doi.org/10.1007/s10346-018-0960-x>.

Gokceoglu C, Aksoy H (1996) Landslide susceptibility mapping of the slopes in the residual soils of the Mengen region (Turkey) by deterministic stability analyses and image processing techniques. *Engineering Geology*. 44 (1-4):147-161. [https://doi.org/10.1016/S0013-7952\(97\)81260-4](https://doi.org/10.1016/S0013-7952(97)81260-4)

Gokceoglu C, Ercanoglu M (2001) Heyelan duyarlılık haritalarının hazırlanmasında kullanılan parametrelerle iliskin belirsizlikler. *Yerbilimleri*. 23, 189–206.

Gokceoglu C, Yurur MT, Kocaman S, Nefeslioglu HA, Durmaz M, Tavus B, Karakas G, Buyukdemircioglu M, Atasoy K, Can R, Yalcin I (2020) Investigation of Elazig Sivrice Earthquake (24 January 2020, Mw=6.8) Employing Radar Interferometry and Stereo Airphoto Photogrammetry. *Hacettepe University, Engineering Faculty, Geomatics and Geological Engineering Departments*, 51p, DOI: 10.13140/RG.2.2.19673.88167.

Guo XY, Fu BH, Du J, Shi PL, Li JX, Li Z, Du J, Chen Q, Fu H (2021) Monitoring and Assessment for the Susceptibility of Landslide Changes After the 2017 Ms 7.0 Jiuzhaigou Earthquake Using the Remote Sensing Technology. *Front Earth Sci*, 9, 633117. <https://doi.org/10.3389/feart.2021.633117>.

Goorabi A (2020) Detection of landslide induced by large earthquake using InSAR coherence techniques – Northwest Zagros, Iran. *Egypt J Remote Sens Space Sci*, 23, 195-

205. <https://doi.org/10.1016/j.ejrs.2019.04.002>.

Gruen A, Akca D (2005) Least squares 3D surface and curve matching. ISPRS J. Photogramm. Remote Sens. 59, 151–174.

Harmouzi H, Nefeslioglu HA, Rouai M, Sezer EA, Dekayir A, Gokceoglu C (2019) Landslide susceptibility mapping of the Mediterranean coastal zone of Morocco between Oued Laou and El Jebha using artificial neural networks (ANN). Arab J Geosci. 12, 696. <https://doi.org/10.1007/s12517-019-4892-0>.

Havenith HB, Strom A, Caceres F, Pirard E (2006) Analysis of landslide susceptibility in the Suusamyr region, Tien Shan: statistical and geotechnical approach. Landslides. 3: 39-50, DOI: 10.1007/s10346-005-0005-0

Jain AK, Mao J, Mohiuddin KM (1996) Artificial neural networks: A tutorial. Computer, 29(3): 31-44. DOI: 10.1109/2.485891

Jenks GF (1967) The data model concept in statistical mapping. Int. Yearb. Cartogr. 7, 186–190.

Nowicki Jessee MA, Hamburger MW, Ferrara MR, McLean A, FitzGerald C (2020) A global dataset and model of earthquake-induced landslide fatalities. Landslides, 17, 1363-1376.

<https://doi.org/10.1007/s10346-020-01356-z>.

Karakas G, Can R, Kocaman S, Nefeslioglu HA, Gokceoglu C (2020). Landslide susceptibility mapping with random forest model for Ordu, Turkey. ISPRS - International Archives of the Photogrammetry, Remote Sensing and Spatial Information Sciences. vol. XLIII-B3-2020, pp. 1229–1236.

Karakas G, Nefeslioglu HA, Kocaman S, Buyukdemircioglu M, Yurur MT, Gokceoglu C (2021 a). Derivation of earthquake-induced landslide distribution using aerial photogrammetry: the 24 January 2020 Elazig (Turkey) Earthquake. Landslides. DOI: 10.1007/s10346-021-01660-2.

Karakas G, Kocaman S, Gokceoglu C (2021 b) Aerial Photogrammetry and Machine Learning Based Regional Landslide Susceptibility Assessment for an Earthquake Prone Area in Turkey. Int Arch Photogramm Remote Sens Spat Inf Sci - ISPRS Arch, 43-B3-2021, 713–720.  
<https://doi.org/10.5194/isprs-archives-XLIII-B3-2021-713-2021>.

Keskin I (2002) 1:100.000 scale Turkish geological maps, L42 Quadrangle. Publication of General Directorate of the Mineral Research and Exploration, 37p.

Kingma DP, Ba J (2014) Adam: A Method for Stochastic Optimization. *CoRR*, <abs/1412.6980>. <https://arxiv.org/pdf/1412.6980.pdf> [last accessed on 31 Mar 2021]

Kocaman S, Tavus B, Nefeslioglu HA, Karakas G, Gokceoglu C (2020) Evaluation of Floods and Landslides Triggered by a Meteorological Catastrophe (Ordu, Turkey, August 2018) Using Optical and Radar Data. Geofluids. Article ID 8830661, <https://doi.org/10.1155/2020/8830661>

Kumar S, Gupta V, Kumar P, Sundriyal, YP (2021) Coseismic landslide hazard assessment for the future scenario earthquakes in the Kumaun Himalaya, India. *B Eng Geol Environ.* <https://doi.org/10.1007/s10064-021-02267-6>.

Li C, Su L (2021) Influence of critical acceleration model on assessments of potential earthquake-induced landslide hazards in Shimian County, Sichuan Province, China. *Landslides.* <https://doi.org/10.1007/s10346-020-01578-1>

Li F, Torgoev I, Zaredinov D, Li M, Talipov B, Belousova A, Kunze C, Schneider P (2021) Influence of Earthquakes on Landslide Susceptibility in a Seismic Prone Catchment in Central Asia. *Appl Sci*, 11, 3768. <https://doi.org/10.3390/app11093768>.

Liu Y, Zhang W, Zhang Z, Xu Q, Li W (2021) Risk Factor Detection and Landslide Susceptibility Mapping Using Geo-Detector and Random Forest Models: The 2018 Hokkaido Eastern Iburi Earthquake. *Remote Sens*, 13, 1157. <https://doi.org/10.3390/rs13061157>.

Mahalingama R, Kim B (2021) Factors Affecting Occurrence of Landslides Induced by the M7.8 April 2015, Nepal Earthquake. *KSCE Journal of Civil Engineering*, 25(1), 78-91, <https://doi.org/10.1007/s12205-020-0508-1>.

Marano KD, Wald DJ, Allen TI (2010) Global earthquake casualties due to secondary effects: a quantitative analysis for improving rapid loss analyses. *Nat Hazards*, 52(2), 319–328. <https://doi.org/10.1007/s11069-009-9372-5>.

Medina V, Hürlimann M, Guo Z, Lloret A, Vaunat J (2021) Fast physically-based model for rainfall-induced landslide susceptibility assessment at regional scale. *Catena*, 201, 105213, <https://doi.org/10.1016/j.catena.2021.105213>

Moore ID, Grayson RB, Ladson AR (1991) Digital terrain modeling: A review of hydrological, geomorphological, and biological applications. *Hydrol. Process.* 5, 3–30.

Nayek PS, Gade M (2021) Seismic landslide hazard assessment of central seismic gap region of Himalaya for a Mw 8.5 scenario event. *Acta Geophysica*, <https://doi.org/10.1007/s11600-021-00572-y>.

Nefeslioglu HA, San BT, Gokceoglu C, Duman TY (2012) An assessment on the use of Terra ASTER L3A data in landslide susceptibility mapping. *International Journal of Applied Earth Observation and Geoinformation.* 14 (1: 40-60, DOI: 10.1016/j.jag.2011.08.005

Newmark NM (1965) Effects of earthquakes on dams and embankments. *Geotechnique*.15(2):139–160

Pradhan B, Sezer EA, Gokceoglu C, Buchroithner MF (2010) Landslide Susceptibility Mapping by Neuro-Fuzzy Approach in a Landslide-Prone Area (Cameron Highlands, Malaysia). *IEEE Trans. Geosci. Remote Sens.* 48 (12): 4164-4177, DOI: 10.1109/TGRS.2010.2050328

Pourghasemi H, Pradhan B, Gokceoglu C, Moezzi, KD (2013) A comparative assessment of prediction capabilities of Dempster-Shafer and Weights-of-evidence models in landslide susceptibility mapping using GIS. *Geomat Nat Haz Risk*, 4(2), 93-118, 10.1080/19475705.2012.662915

Qi T, Zhao Y, Meng X, Chen G, Dijkstra T (2021) AI-Based Susceptibility Analysis of Shallow Landslides Induced by Heavy Rainfall in Tianshui, China. *Remote Sens*, 13 (9), 1819, <https://doi.org/10.3390/rs13091819>.

Rodríguez-Peces MJ, García-Mayordomo J, Azañón JM, Jabaloy A (2014) GIS application for regional assessment of seismically induced slope failures in the Sierra Nevada Range, South Spain, along the Padul Fault. *Environ Earth Sci*. 72, 2423–2435. <https://doi.org/10.1007/s12665-014-3151-7>

Sahana M, Pham BT, Shukla M, Costache R, Thu DX, Chakrabortty R, Satyam N, Nguyen HD, Phong TV, Le HV. et. al. (2020) Rainfall induced landslide susceptibility mapping using novel hybrid soft computing methods based on multi-layer perceptron neural network classifier, Geocarto International. DOI: [10.1080/10106049.2020.1837262](https://doi.org/10.1080/10106049.2020.1837262).

Scikit-learn. 2021. Python Library.

[https://scikit-learn.org/stable/modules/neural\\_networks\\_supervised.html#multi-layer-perceptron](https://scikit-learn.org/stable/modules/neural_networks_supervised.html#multi-layer-perceptron) [last accessed on 20.07.2021]

Sevgen E, Kocaman S, Nefeslioglu HA, Gokceoglu C (2019) A Novel Performance Assessment Approach Using Photogrammetric Techniques for Landslide Susceptibility Mapping with Logistic Regression, ANN and Random Forest. *Sensors*. 19:3940, doi:10.3390/s19183940.

Shinoda M, Miyata Y (2017) Regional landslide susceptibility following the Mid NIIGATA prefecture earthquake in 2004 with NEWMARK'S sliding block analysis. *Landslides*. 14, 1887–1899. <https://doi.org/10.1007/s10346-017-0833-8>

Shinoda M, Miyata Y, Kurokawa U, Kondo K (2019) Regional landslide susceptibility following the 2016 Kumamoto earthquake using back-calculated geomaterial strength parameters. *Landslides*. 16, 1497–1516. <https://doi.org/10.1007/s10346-019-01171-1>

Tatar O, Sözbilir H, Koçbulut F, Bozkurt E, Aksoy E, Eski S, Özmen B, Alan H, Metin Y (2020) Surface deformations of 24 January 2020 Sivrice (Elazığ)–Doğanyol (Malatya) earthquake ( $M_w = 6.8$ ) along the Pütürge segment of the East Anatolian Fault Zone and its comparison with Turkey's 100-year-surface ruptures. *Med Geosci Rev*, 2, 385–410. <https://doi.org/10.1007/s42990-020-00037-2>.

Temür R, Damcı E, Öncü-Davas S, Öser C, Sarçın S, Şekerci Ç (2021) Structural and geotechnical investigations on Sivrice earthquake ( $M_w = 6.8$ ), January 24, 2020. *Nat Hazards*, 106, 401–434. <https://doi.org/10.1007/s11069-020-04468-w>.

Tsou CY, Chigira M, Higaki D, Sato G, Yagi H, Sato HP, Wakai A, Dangol V, Amatya SC, Yatagai A (2018) Topographic and geologic controls on landslides induced by the 2015 Gorkha earthquake and its aftershocks: an example from the Trishuli Valley, central Nepal. *Landslides*, 15:953–965. <https://doi.org/10.1007/s10346-017-0913-9>.

Wang LJ, Guo M, Sawada K, Lin J, Zhang J (2016) A comparative study of landslide susceptibility maps using logistic regression, frequency ratio, decision tree, weights of evidence and artificial neural network. *Geosci. J.* 20, 117–136. <https://doi.org/10.1007/s12303-015-0026-1>.

Wang Z, Liu Q, Liu Y (2020) Mapping Landslide Susceptibility Using Machine Learning Algorithms and GIS: A Case Study in Shexian County, Anhui Provience, China. *Symmetry*, 12(12), 1954. <https://doi.org/10.3390/sym12121954>.

Wang X, Li S, Liu H, Liu L, Liu Y, Zeng S, Tang Q (2021) Landslide susceptibility assessment in Wenchuan County after the 5.12 magnitude earthquake. *B Eng Geol Environ*, <https://doi.org/10.1007/s10064-021-02280-9>

Wilson JP, Gallant JC (2000) *Terrain Analysis: Principles and Applications*; John Wiley and Sons, Inc.: Ottawa, ON, Canada.

Wu B, Qiu W, Jia J, Liu N (2020) Landslide Susceptibility Modeling Using Bagging-Based Positive-Unlabeled Learning. *IEEE Geosci Remote*, 18 (5), 766-770, <https://doi.org/10.1109/LGRS.2020.2989497>.

Xie P, Wen H, Ma C, Baise LG, Zhang J (2018) Application and comparison of logistic regression model and neural network model in earthquake induced landslides susceptibility mapping at mountainous region, China. *Geomatics, Natural Hazards and Risk*. 9(1): 501-523, DOI: 10.1080/19475705.2018.1451399

Yanar T, Kocaman S, Gokceoglu C (2020) Use of Mamdani Fuzzy Algorithm for Multi-Hazard Susceptibility Assessment in a Developing Urban Settlement (Mamak, Ankara, Turkey). *ISPRS Int. J. Geo-Inf.* 9, 114.

Yalcin I, Kocaman S, Gokceoglu C (2020 a) Production of Iso-Intensity Map for the Elazig Earthquake (Jan 24, 2020) Using Citizen Collected Geodata. *The International Archives of Photogrammetry, Remote Sensing and Spatial Information Sciences*. 43, 51-56. DOI: 10.5194/isprs-archives-XLIII-B5-2020-51-2020

Yalcin I, Kocaman S, Gokceoglu C (2020 b) A CitSci Approach for Rapid Earthquake intensity mapping: A case study from Istanbul (Turkey). *ISPRS International Journal of Geo-Information*. 9(4): 266. DOI: 10.3390/ijgi9040266

Zakerinejad R, Maerker M (2015) An integrated assessment of soil erosion dynamics with special emphasis on gully erosion in the Mazayjan basin, southwestern Iran. *Nat. Hazards*. 79, 25–50, doi:10.1007/s11069- 015-1700-3.

Zare M, Pourghasemi HR, Vafakhah M, Pradhan B (2013) Landslide susceptibility mapping at Vaz Watershed (Iran) using an artificial neural network model: a comparison between multilayer perceptron (MLP) and radial basic function (RBF) algorithms. *Arab J Geosci.* 6, 2873–2888. <https://doi.org/10.1007/s12517-012-0610-x>

Zhao B, Li W, Wang Y, Lu J, Li X (2019) Landslides triggered by the Ms 6.9 Nyingchi earthquake, China (18 November 2017): analysis of the spatial distribution and occurrence factors. *Landslides*, 16, 765–776. <https://doi.org/10.1007/s10346-019-01146-2>.

Zhou JW, Lu PY, Hao MH (2016) Landslides triggered by the 3 August 2014 Ludian earthquake in China: geological properties, geomorphologic characteristics and spatial distribution analysis, *Geomatics Natural Hazards and Risk*, 7:4, 1219–1241, DOI:[10.1080/19475705.2015.1075162](https://doi.org/10.1080/19475705.2015.1075162)

## Tables

**Table 1. Features and geodata types used as conditioning factors in the study area.**

Category	Features	Data Type	Scale/Resolution	Source
Topographical	Altitude			
	Slope			
	Aspect			
	Plan and Profile Curvature	Grid	5 m	GDM
	SPI			
	TWI			
Geological	Lithology	Polygon	1:100 000	Geological maps published by Akbas et al. (2016)

**Table 2. The model parameters used RF and MLP algorithms**

Model	Parameter and Value
Random Forest	n_estimators=128 criterion='entropy' max_depth=16 min_samples_split=2 min_samples_leaf=4 class_weight='balanced' bootstrap='true'
Multi-layer Perceptron Neural Network	hidden_layer_sizes=100 max_iter=150 solver='adam' learning_rate='adaptive' activation='relu'

Table 3. Statistical summary of elevations and the topographic derivatives in the study area.

Data Part	Parameters	Min	Max	Mean	s	Median
Malatya	Altitude (m)	452.25	2171.94	1145.94	338.32	1103.76
	Slope (°)	0.00	87.40	20.99	11.17	20.17
	Aspect (°)	0.00	360.00	171.92	101.41	167.94
	Plan cur.	-0.772	0.841	0.002	0.0103	0.007
	Profile cur.	-0.857	0.683	-0.002	0.009	0.003
	TWI	0.001	24.081	5.736	2.178	5.268
Elazig	SPI	0.004	23.639	8.327	1.851	8.255
	Altitude (m)	552.65	2030.88	1223.46	361.08	1204.29
	Slope (°)	0.00	87.57	23.13	11.31	22.62
	Aspect (°)	0.00	360.00	190.45	99.71	192.26
	Plan cur.	-0.299	0.369	0.001	0.011	0.006
	Profile cur.	-0.363	0.352	-0.001	0.009	0.002
	TWI	0.011	24.124	5.646	2.177	5.176
	SPI	0.005	23.135	8.497	1.826	8.394

**Table 4. Statistical summary of the altitudes and the topographic derivatives inside the landslide inventory (all activity types).**

Data Part	Parameters	Min	Max	Mean	s	Median
Malatya	Altitude (m)	679.00	1737.28	1155.53	247.90	1158.83
	Slope (°)	0.06	71.53	25.00	9.35	24.84
	Aspect (°)	0.00	360.00	157.47	59.45	156.39
	Plan cur.	-0.111	0.075	-0.004	0.011	0.002
	Profile cur.	-0.149	0.087	-0.001	0.009	0.002
	TWI	0.901	20.718	5.670	1.699	5.428
	SPI	0.795	20.069	9.063	1.608	8.920
	Altitude (m)	678.032	1845.216	1223.361	255.864	1236.829
Elazig	Slope (°)	0.029	69.230	25.685	9.386	25.813
	Aspect (°)	0.000	360	159.203	53.006	157.630
	Plan cur.	-0.116	0.085	-0.002	0.011	0.004
	Profile cur.	-0.098	0.082	-0.001	0.009	0.006
	TWI	0.533	20.821	5.691	1.693	5.452
	SPI	0.275	18.449	9.147	1.571	9.020

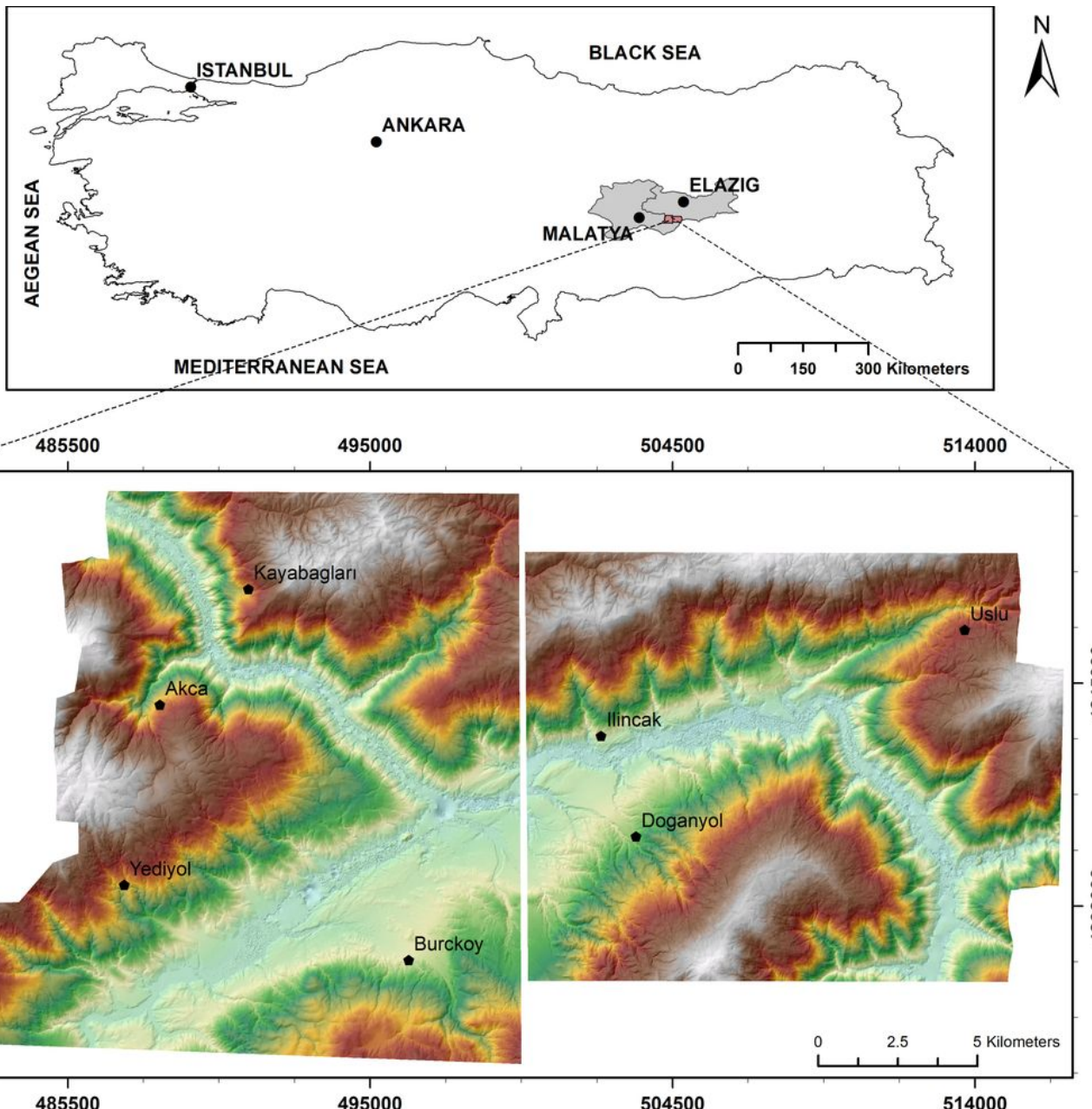
**Table 5. The landslide probability distributions obtained from RF and MLP algorithms.**

Data Part	Method	Class	Probability Range (%)	Area (km <sup>2</sup> )	Percentage (%)
<b>Malatya</b>	RF	Very High	76-100	39.87	15.72
		High	55-76	36.94	14.57
		Moderate	33-55	32.98	13.01
		Low	13-33	42.51	16.77
		Very Low	0-13	101.26	39.94
	MLP	Very High	75-100	27.63	10.90
		High	53-75	35.44	13.98
		Moderate	32-53	41.33	16.30
		Low	13-32	50.55	19.94
		Very Low	0-13	98.61	38.89
<b>Elazig</b>	RF	Very High	79-100	31.65	15.52
		High	59-79	32.51	15.94
		Moderate	36-59	28.51	13.98
		Low	15-36	30.36	14.88
		Very Low	0-15	80.94	39.68
	MLP	Very High	79-100	33.57	16.46
		High	55-79	26.54	13.01
		Moderate	33-55	31.10	15.25
		Low	13-33	36.57	17.93
		Very Low	0-13	76.20	37.36

**Table 6. Statistical summary of probability results obtained from a total of 69 landslides (L3 and L4).**

Data Part	Model	Landslide type	Min	Max	Mean	s	Median	Area (km <sup>2</sup> )
Malatya	RF	L3	0.29	0.84	0.64	0.12	0.66	1.31
		L4	0.25	0.71	0.53	0.12	0.54	0.02
	MLP	L3	0.14	0.76	0.47	0.13	0.47	1.31
		L4	0.17	0.63	0.41	0.12	0.43	0.02
Elazig	RF	L3	0.17	0.84	0.62	0.14	0.64	6.84
		L4	0.45	0.88	0.74	0.11	0.76	0.01
	MLP	L3	0.10	0.82	0.56	0.14	0.58	6..84
		L4	0.28	0.79	0.53	0.11	0.52	0.01

## Figures

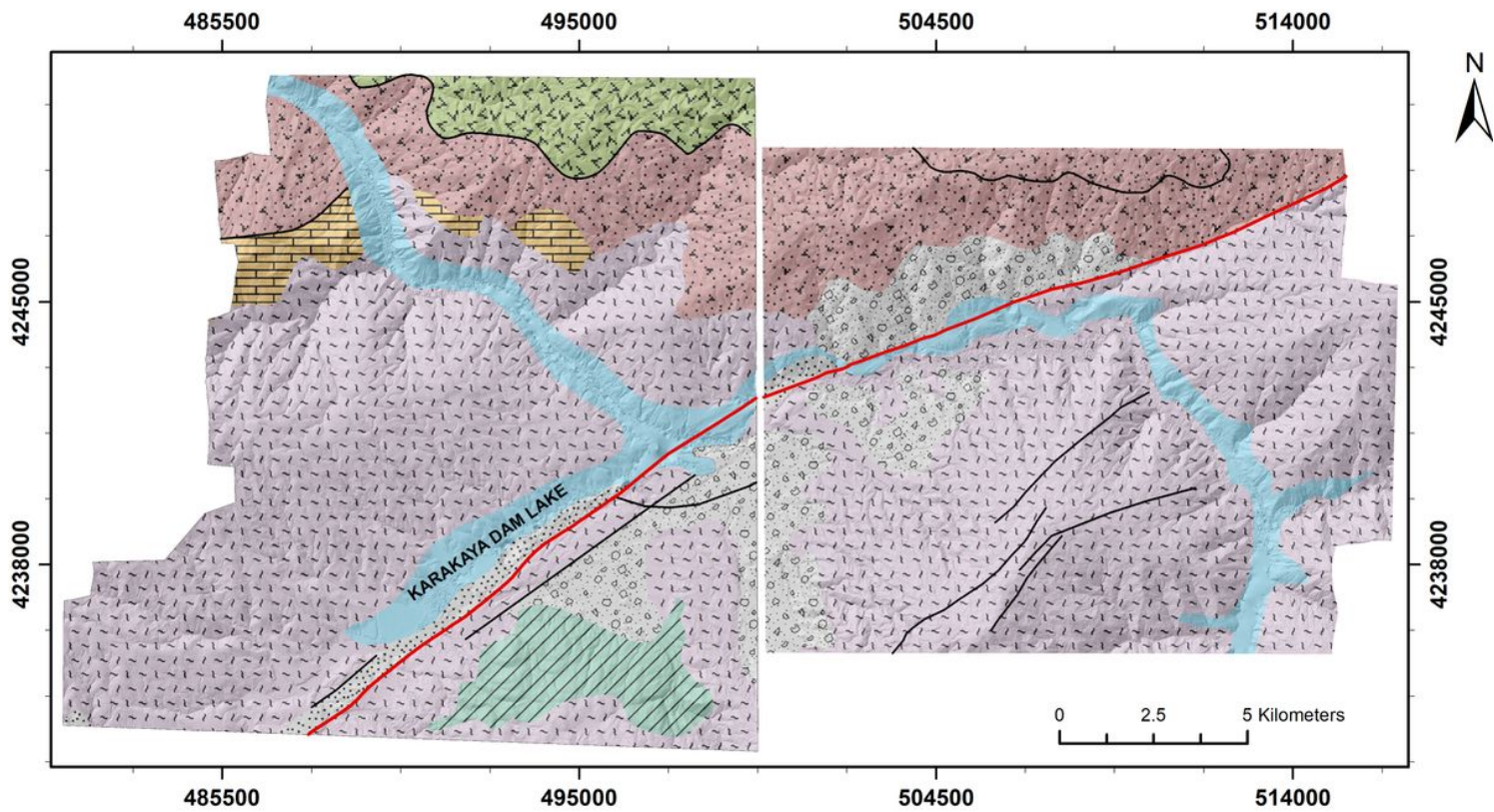


#### Legend

Altitude Malatya Part	Altitude Elazig Part	
Value	Value	
High : 2171.94	High : 2030.88	
Low : 452.247	Low : 552.654	

**Figure 1**

The location map of the study area with the DSM produced for Malatya (left, from year 2017) and Elazig (right, from year 2018) parts.

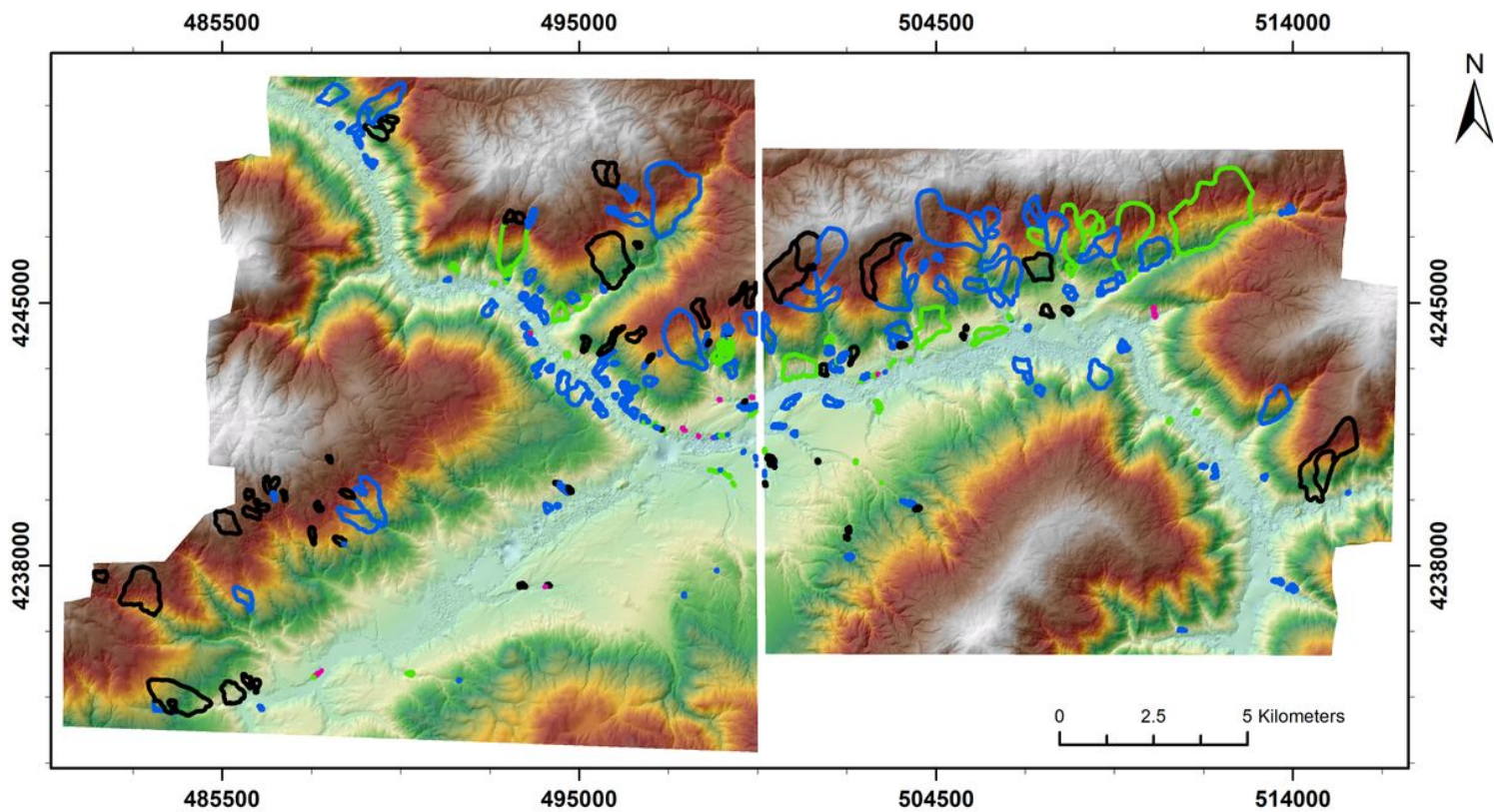


### Legend

<b>Lithology</b>			
Alluvium	Dotted pattern	Maden Complex	— EAFZ
Unconsolidated Gravel, Sand, Silt, Clay	Cross-hatch pattern	Pre-Cenozoic Magmatic Rocks	— Fault
Neritic Limestone	Brick pattern	Puturge Metamorphites	
	Diagonal hatching	Marble	

**Figure 2**

The geological map of the study area for Malatya (left) and Elazig (right) parts (Akbas et al. 2016).



### Legend

Altitude Malatya Part	Altitude Elazig Part	Landslides (Activity)
Value	Value	
High : 2171.94	High : 2030.88	1
Low : 452.247	Low : 552.654	2
		3
		4

**Figure 3**

The DSM of the study area for Malatya (left) and Elazig (right) parts produced from pre-event photogrammetric datasets and the landslides classified by the activity type, such as L1: inactive mass movements, L2: active mass movements, L3: areas containing new active zones inside the existing landslide occurred after 2018, L4: newly developed areas after 2018 (triggered by the earthquake) (Karakas et al. 2021 a).

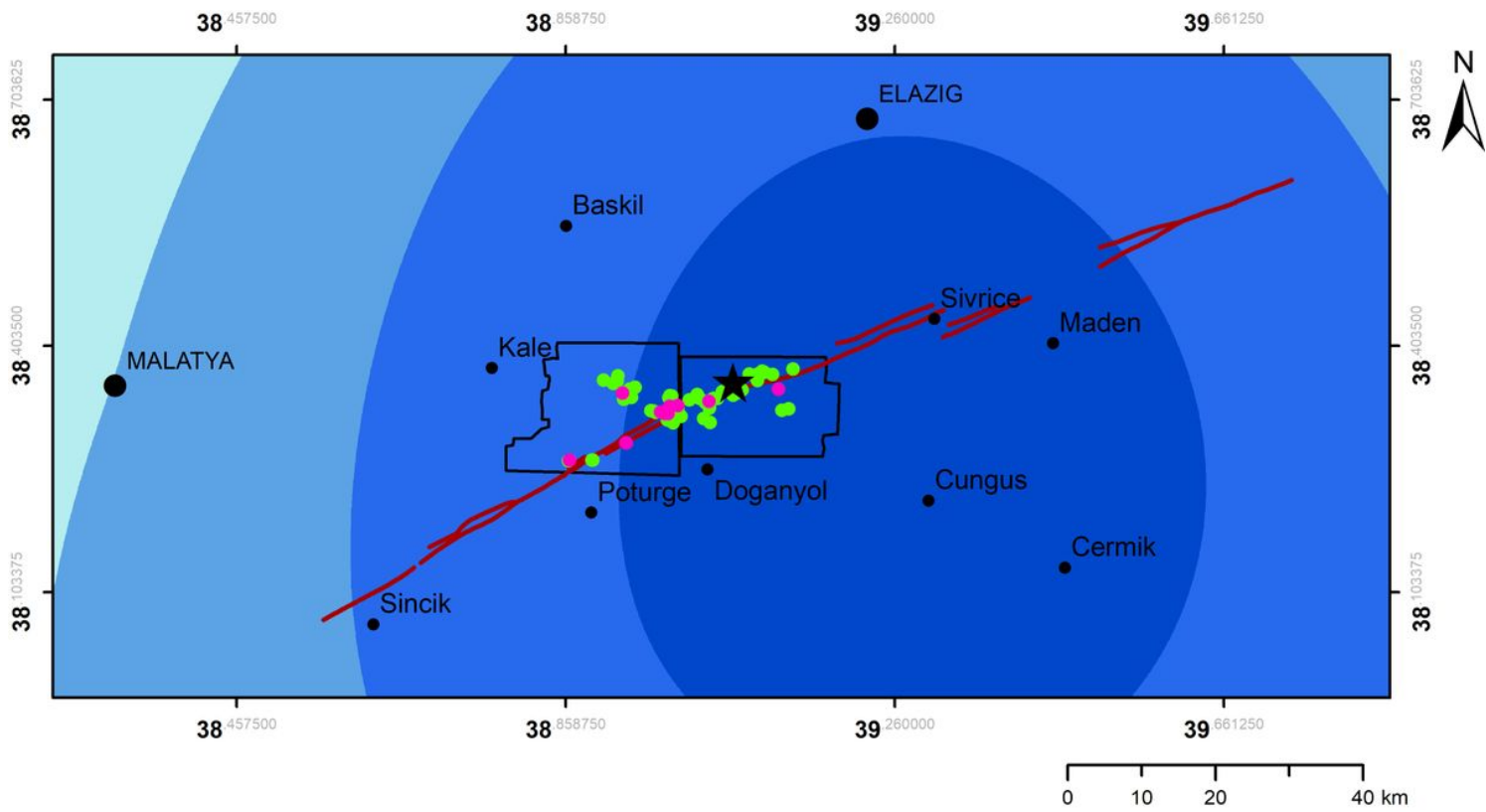


**Figure 4**

The distribution of the landslides on the iso-intensity classes of the Elazig Earthquake produced by Yalcin et al. (2020a).

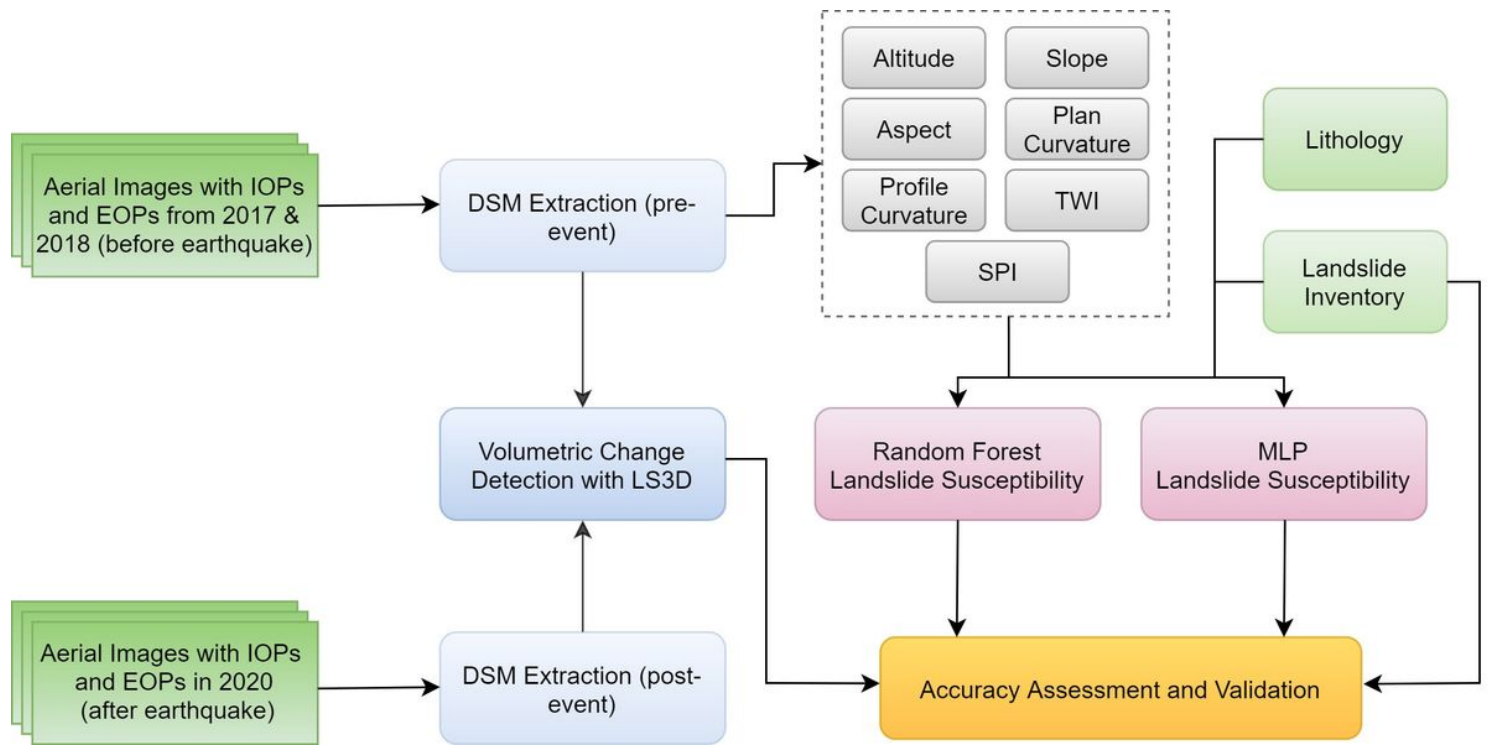


**Figure 5**

The study workflow.

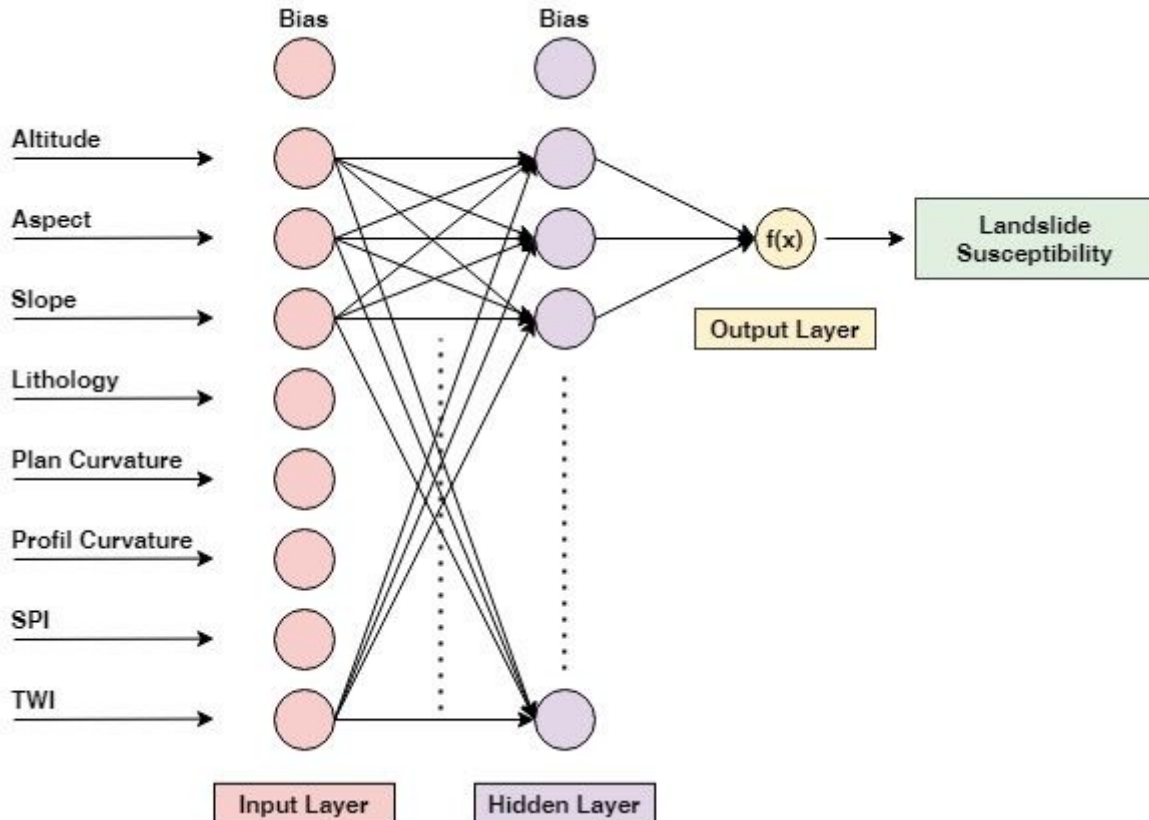


**Figure 6**

The MLP structure used in this study.

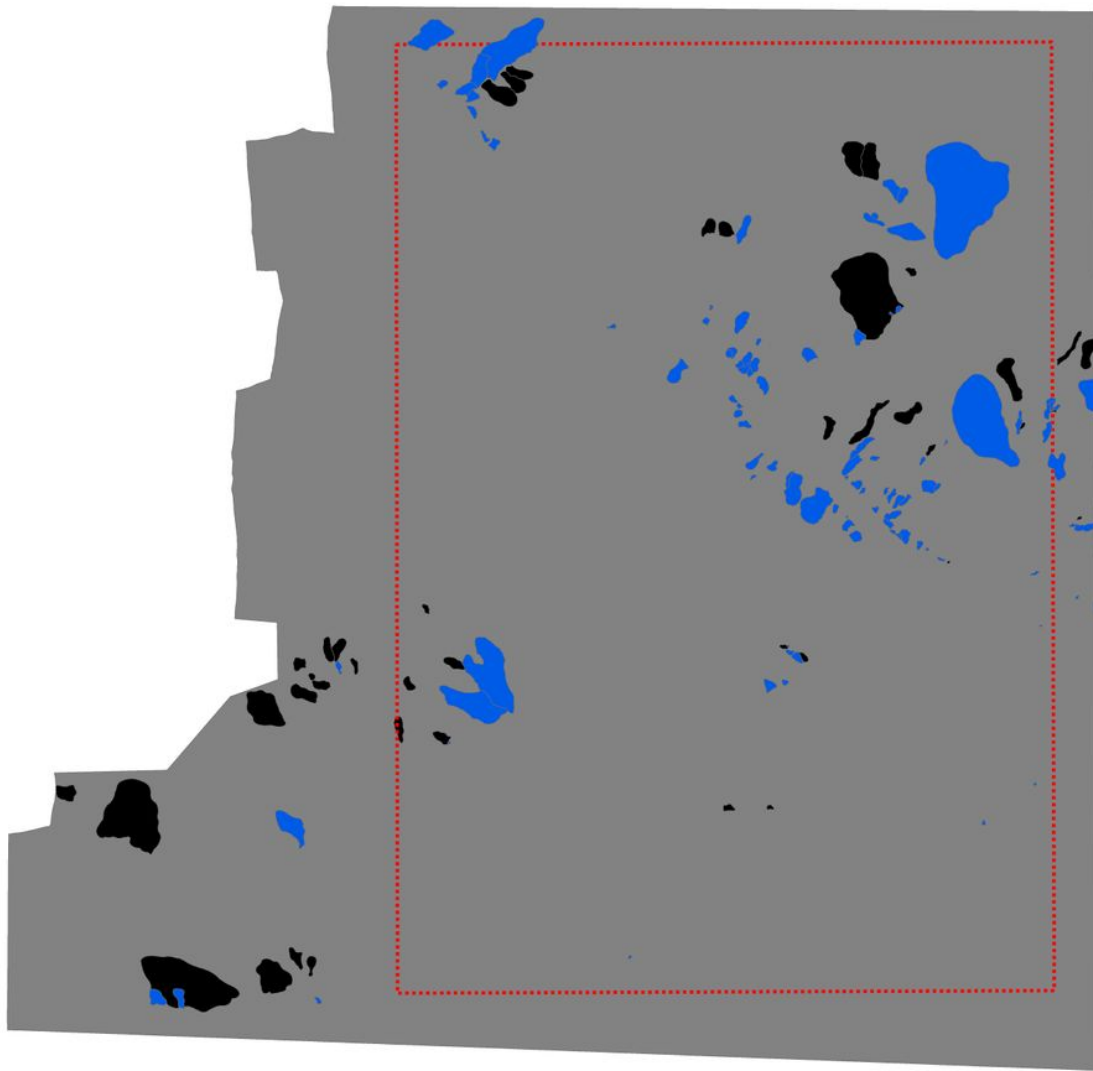


**Figure 7**

The model training area (red rectangle) in the Malatya part with the landslide inventory used for the training (L1 type: black polygons; L2 type: blue polygons).

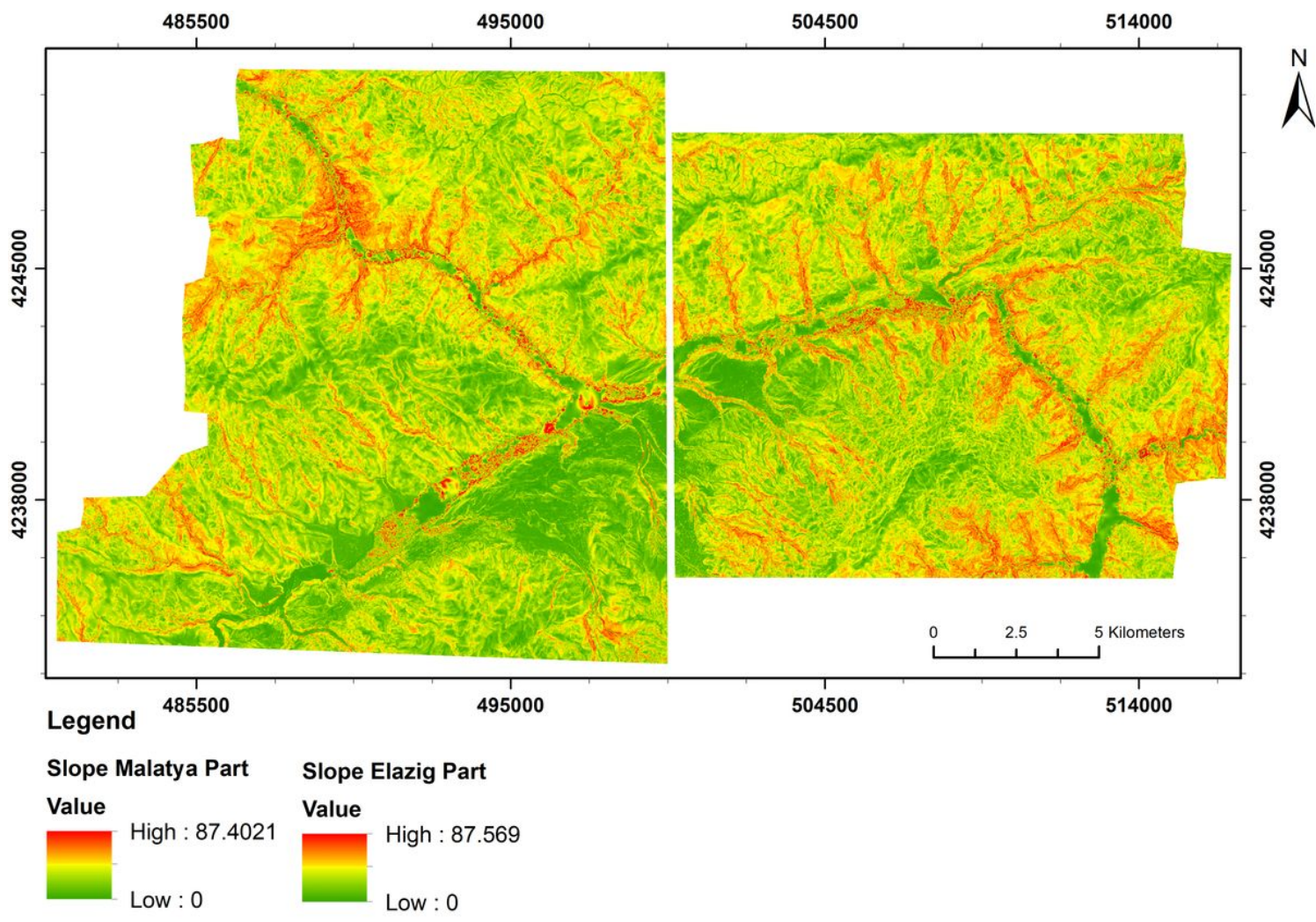
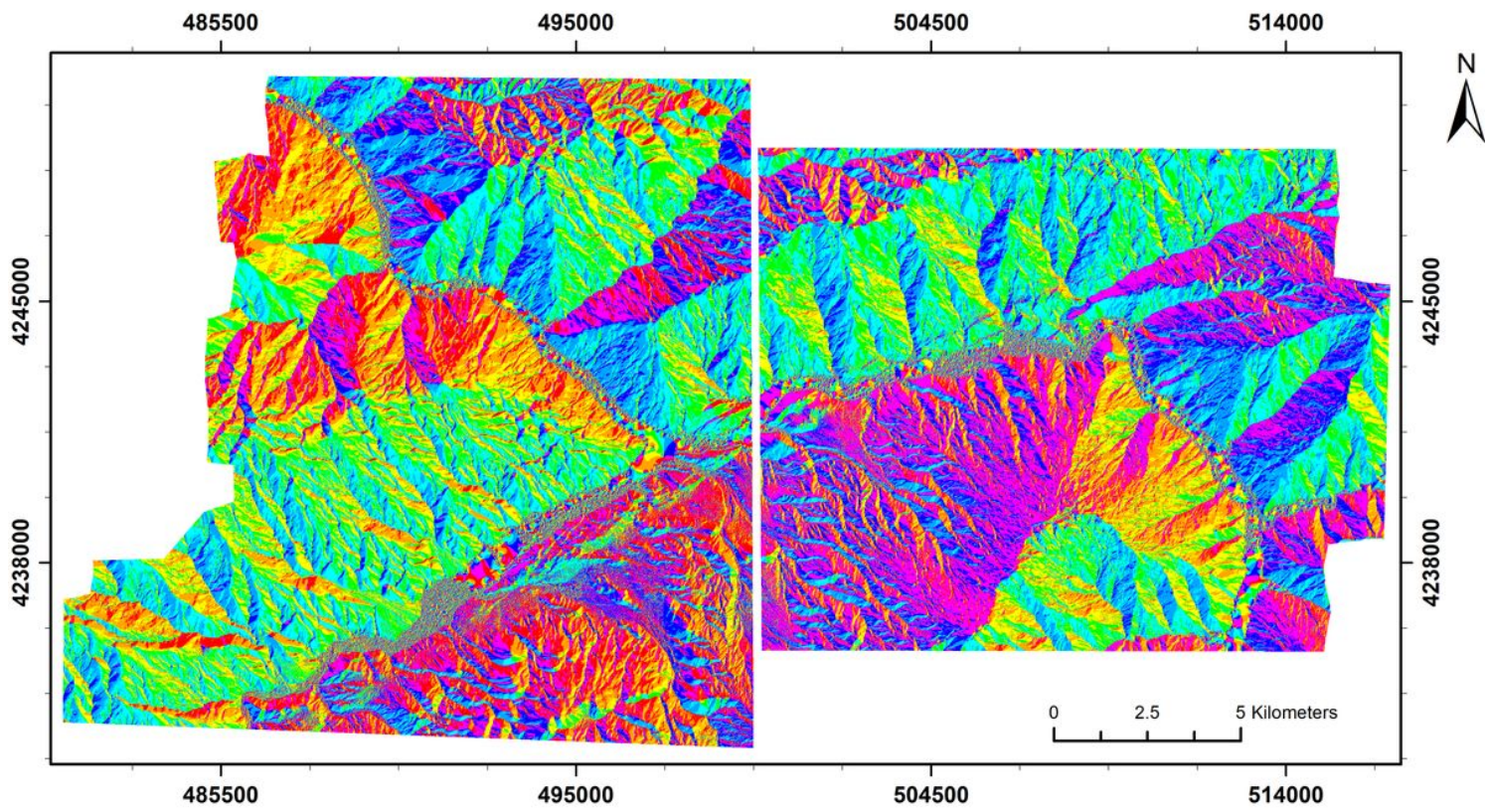


**Figure 8**

The slope map of the study area in degrees.

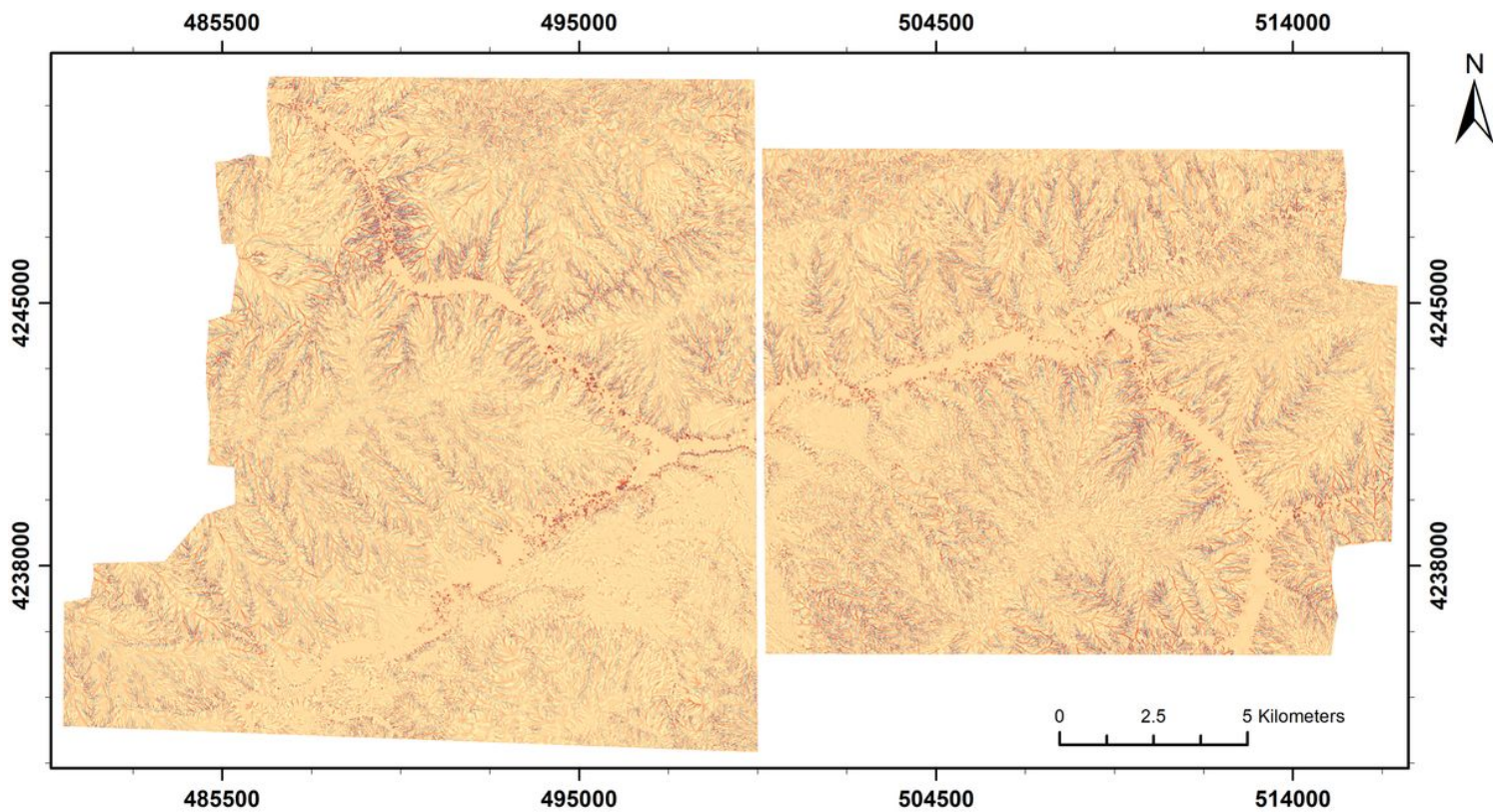


**Legend**

Aspect	<span style="color:red">■</span>	N	<span style="color:yellow">■</span>	E	<span style="color:cyan">■</span>	S	<span style="color:blue">■</span>	W
Flat	<span style="background-color:grey;">■</span>	NE	<span style="color:green">■</span>	SE	<span style="color:lightblue">■</span>	SW	<span style="color:magenta">■</span>	NW

**Figure 9**

The aspect map of the study area as geographical directions.

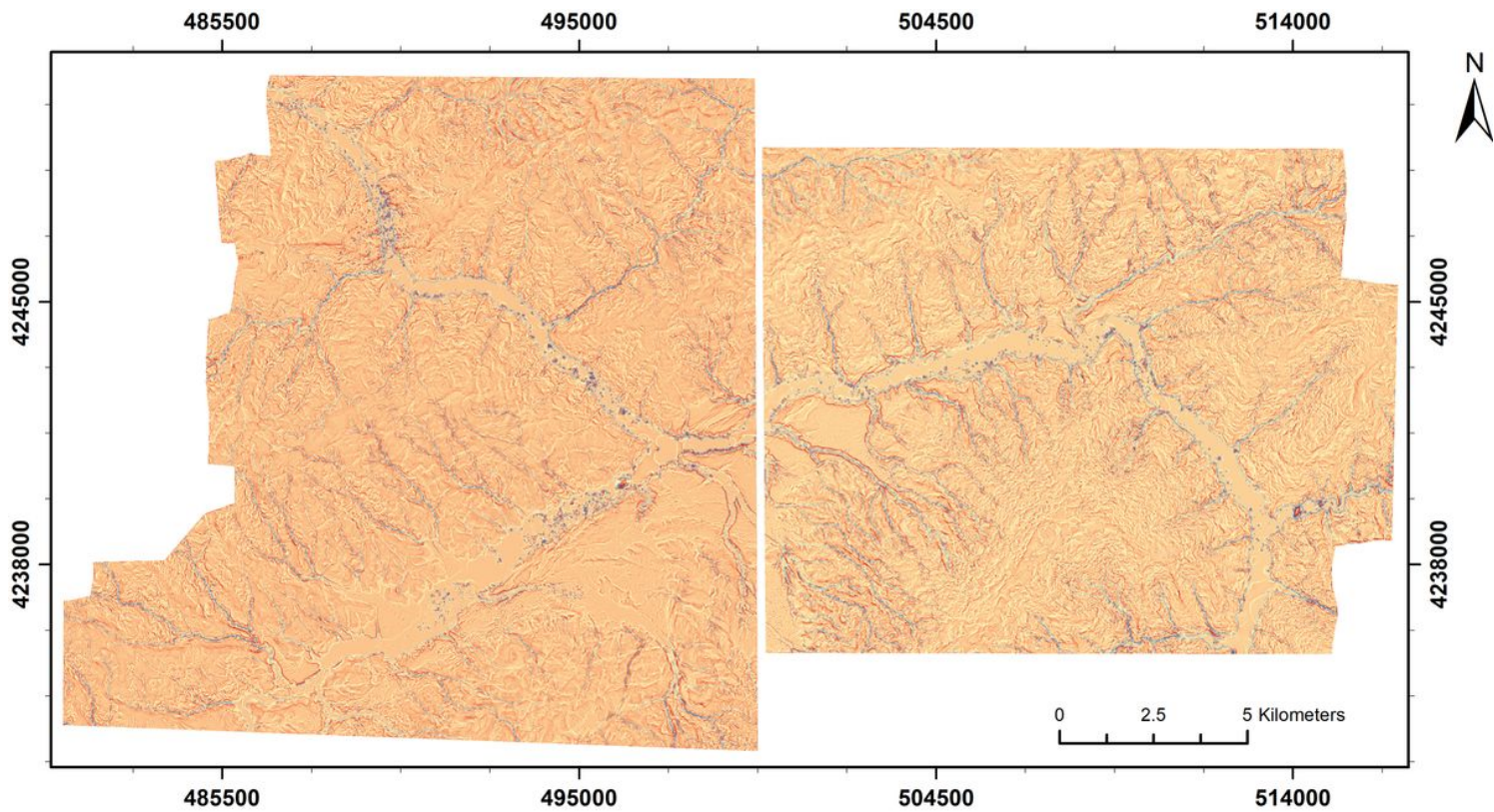


### Legend

Plan Curvature Malatya Part	Plan Curvature Elazig Part
<b>Value</b>	<b>Value</b>
High : 0.841393	High : 0.369105
Low : -0.772343	Low : -0.299658

**Figure 10**

The plan curvature map of the study area.

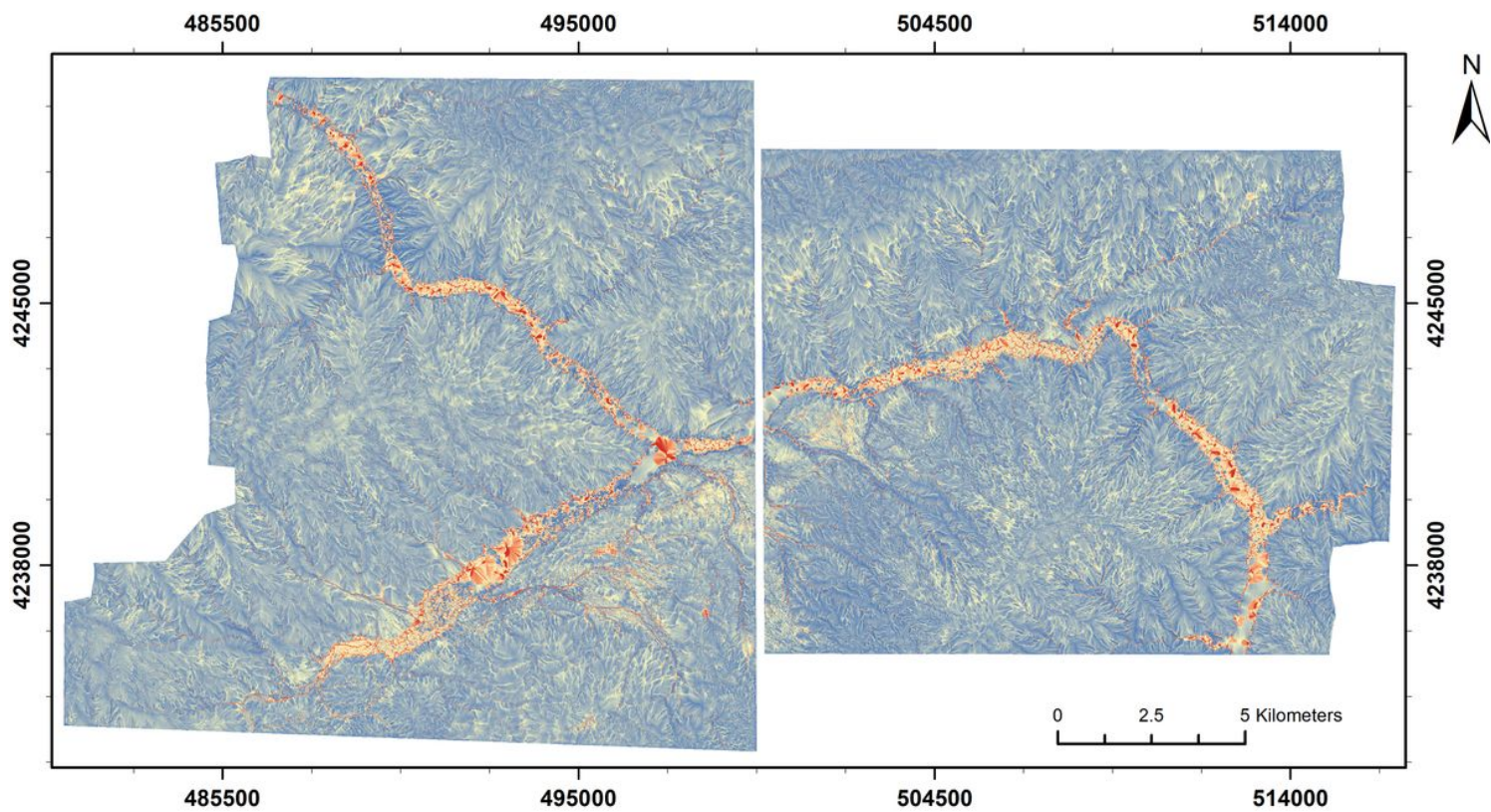


#### Legend

Profile Curvature	Malatya Part	Profile Curvature	Elazig Part
<b>Value</b>		<b>Value</b>	
High : 0.683718		High : 0.352012	
Low : -0.857119		Low : -0.363033	

**Figure 11**

The profile curvature map of the study area.

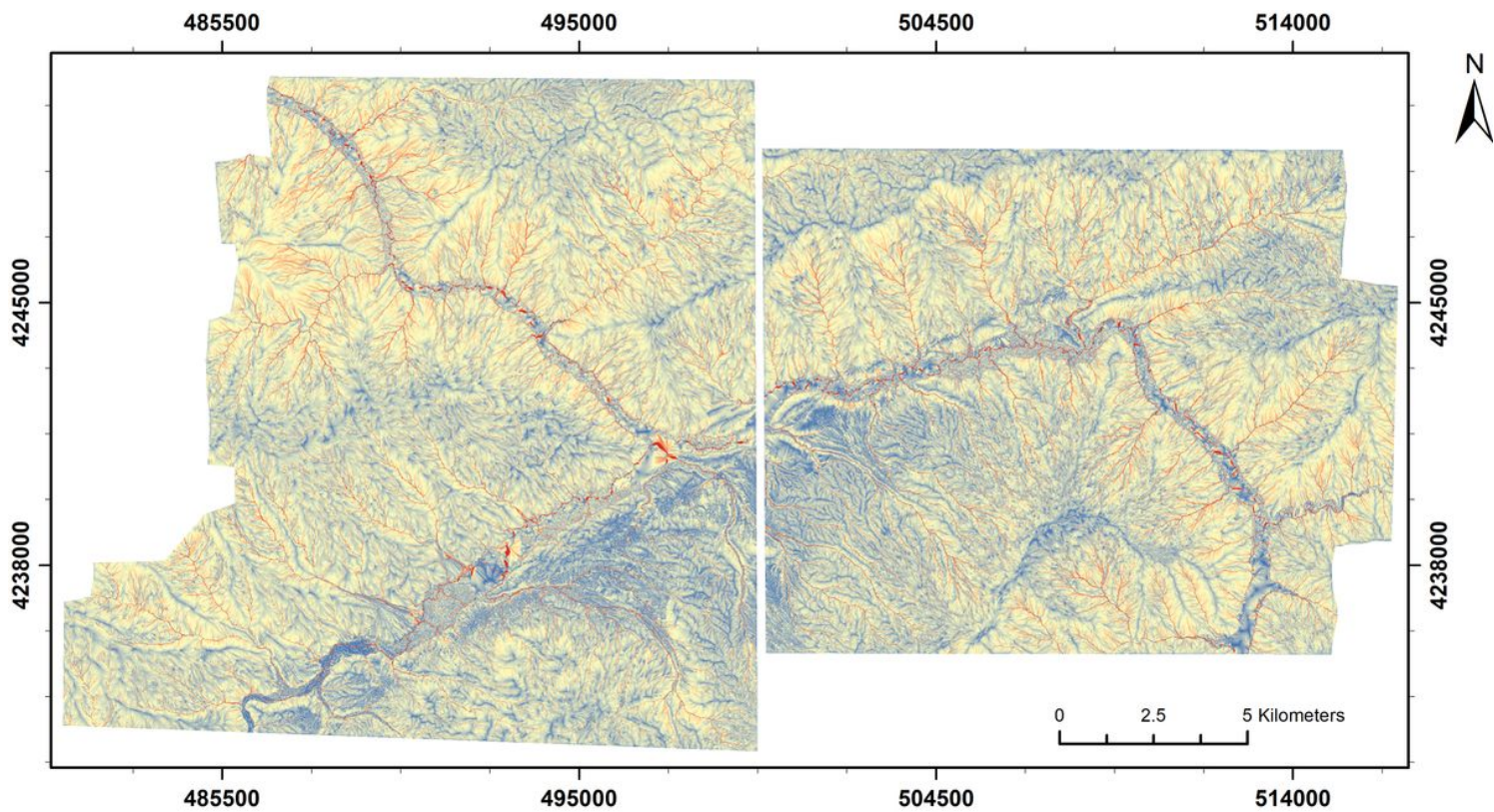


### Legend

TWI Malatya Part		TWI Elazig Part	
Value	Value	Value	Value
High : 24.0818	High : 24.125	Low : 0.0013	Low : 0.0113

**Figure 12**

The TWI map of the study area.



#### Legend

**SPI Malatya Part**

Value	Range
High	: 23.6392
Low	: 0.0044

**SPI Elazig Part**

Value	Range
High	: 23.1354
Low	: 0.0054

**Figure 13**

The SPI map of the study area.

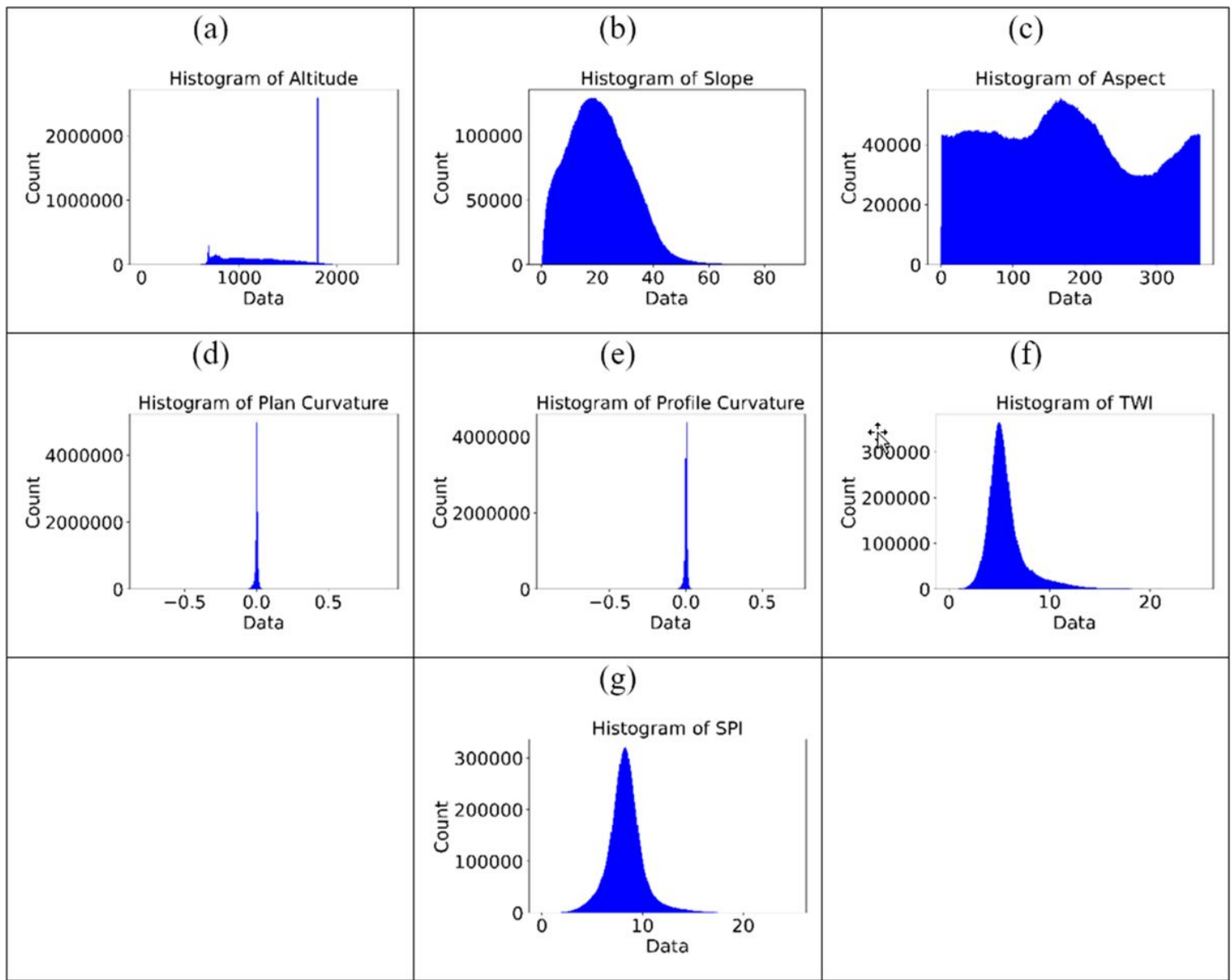


**Figure 14**

Histograms of the altitude values and the topographical features for Malatya part. (a) Altitude, (b) slope, (c) aspect, (d) plan curvature, (e) profile curvature, (f) TWI, and (g) SPI.

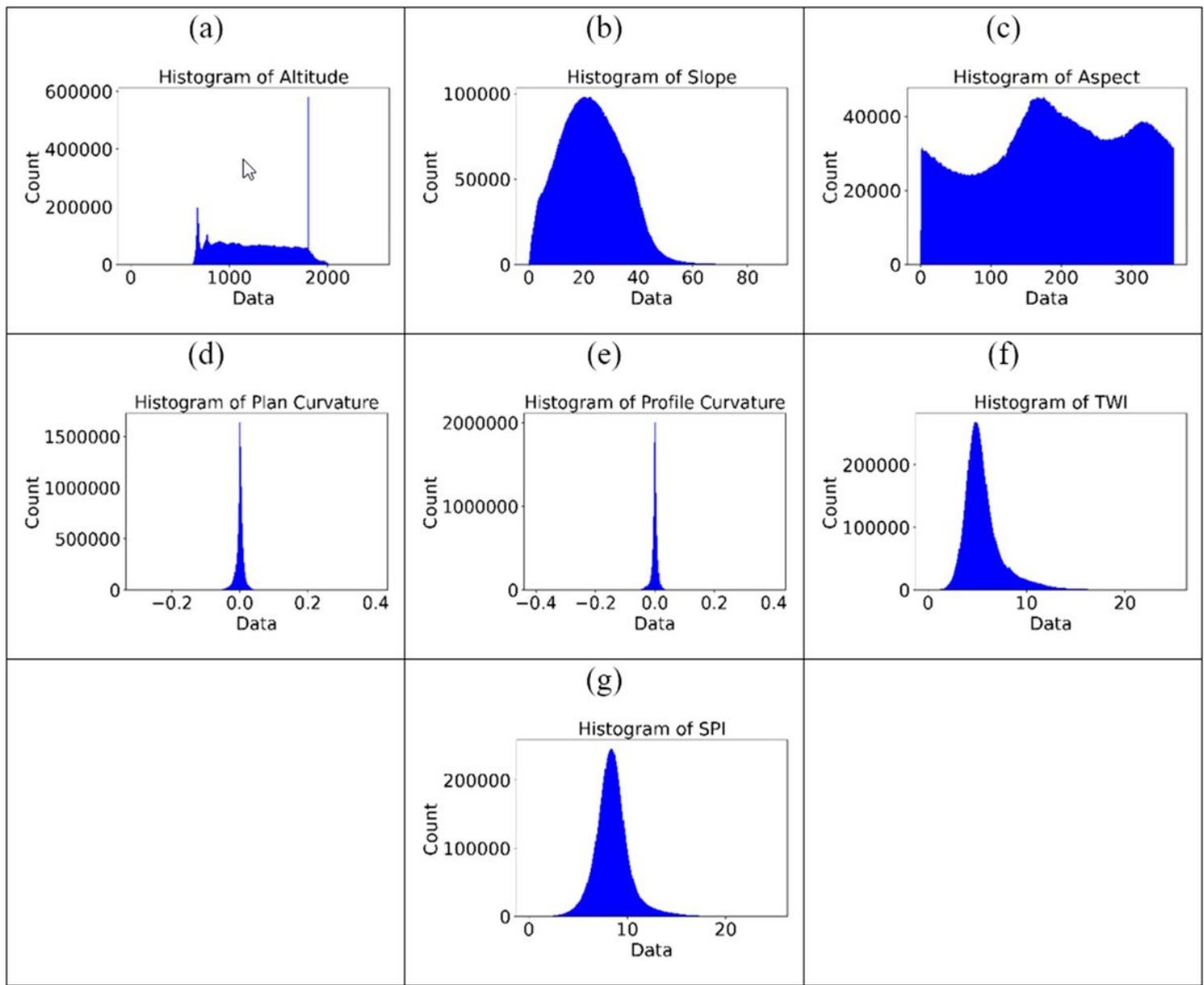


**Figure 15**

Histograms of the altitude values and the topographical features for Elazig part. (a) Altitude, (b) slope, (c) aspect, (d) plan curvature, (e) profile curvature, (f) TWI, and (g) SPI.

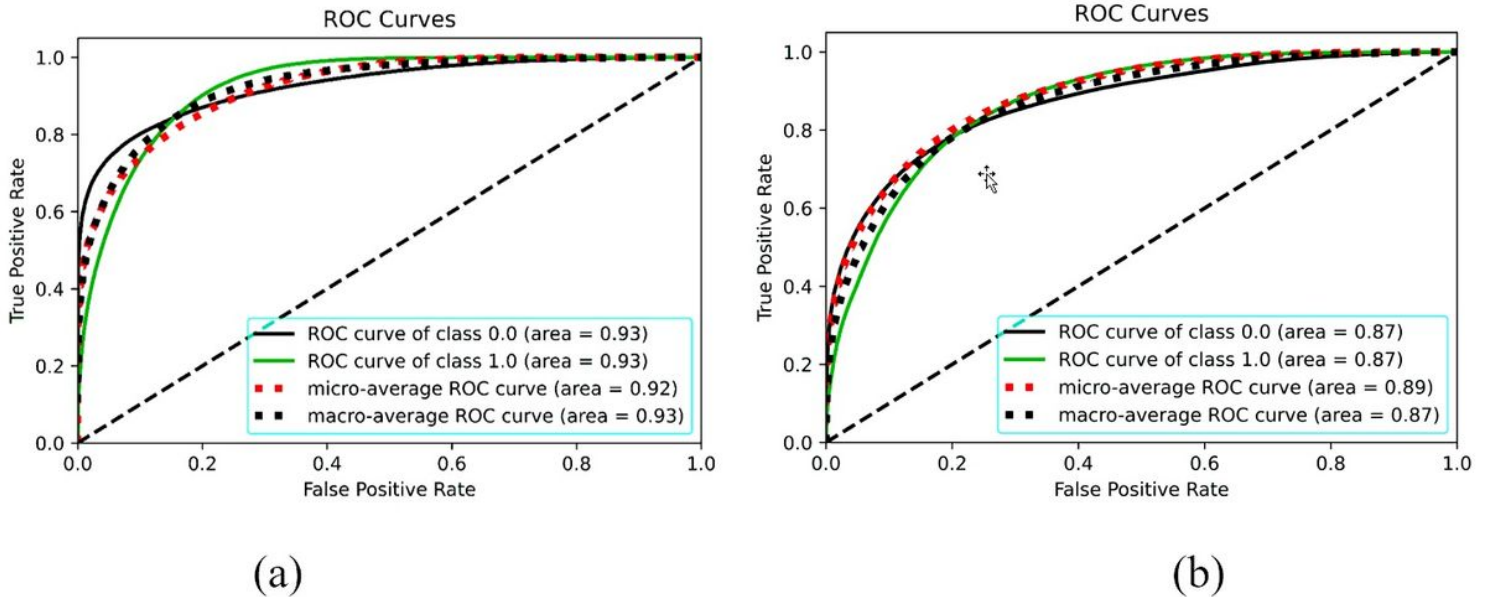
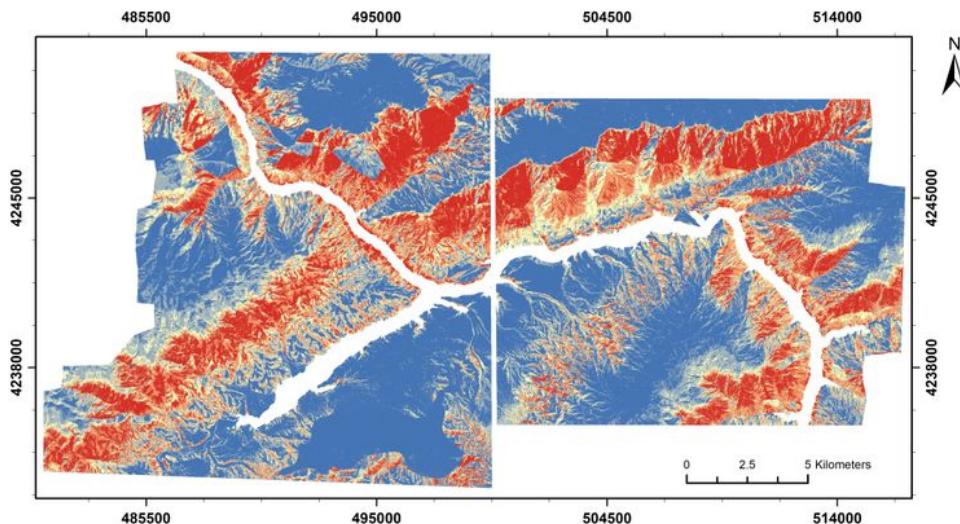


**Figure 16**

ROC curves obtained from the (a) RF and (b) MLP methods using the training and test samples. Class 0.0: non-landslide; Class 1.0: landslide



(a)

(b)

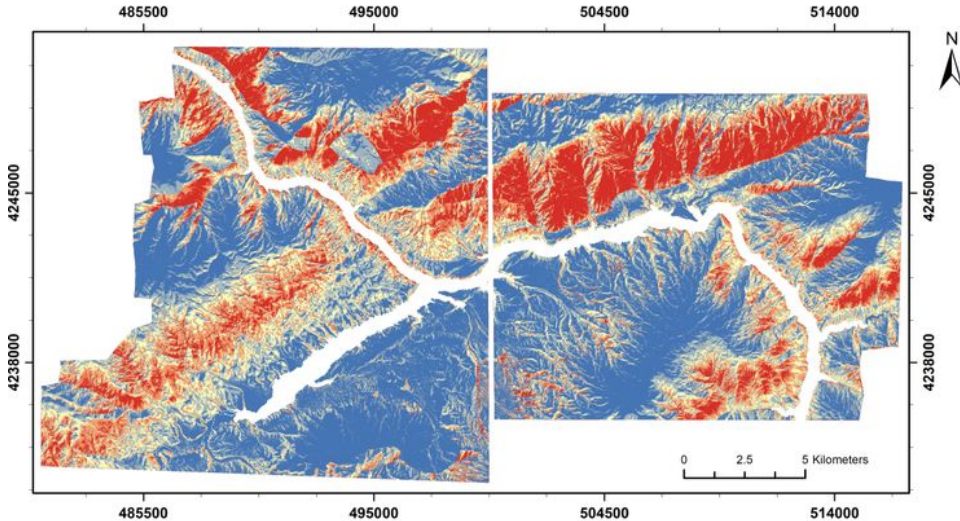
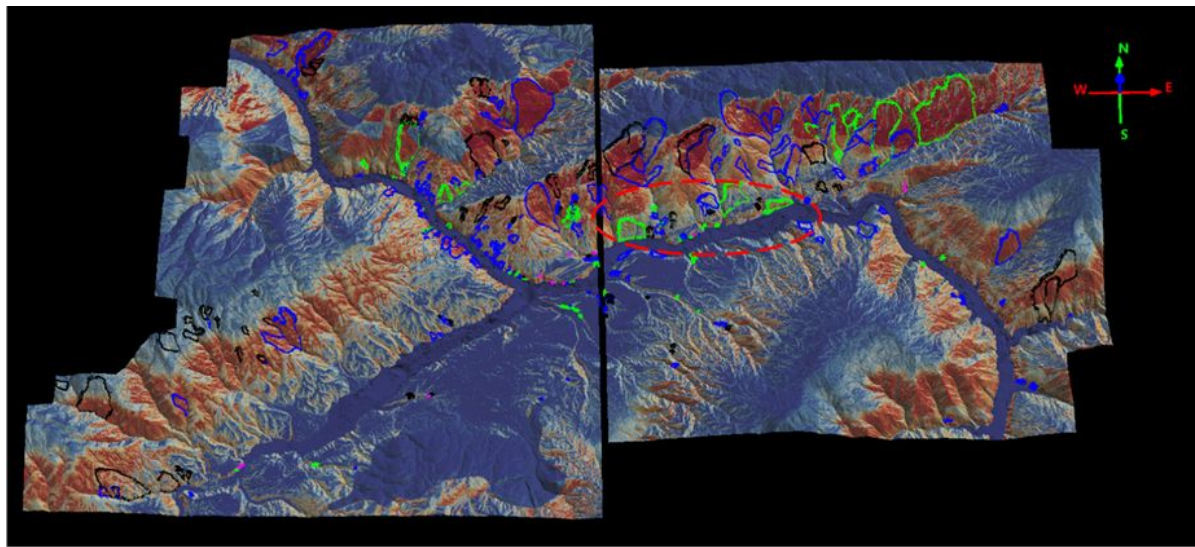
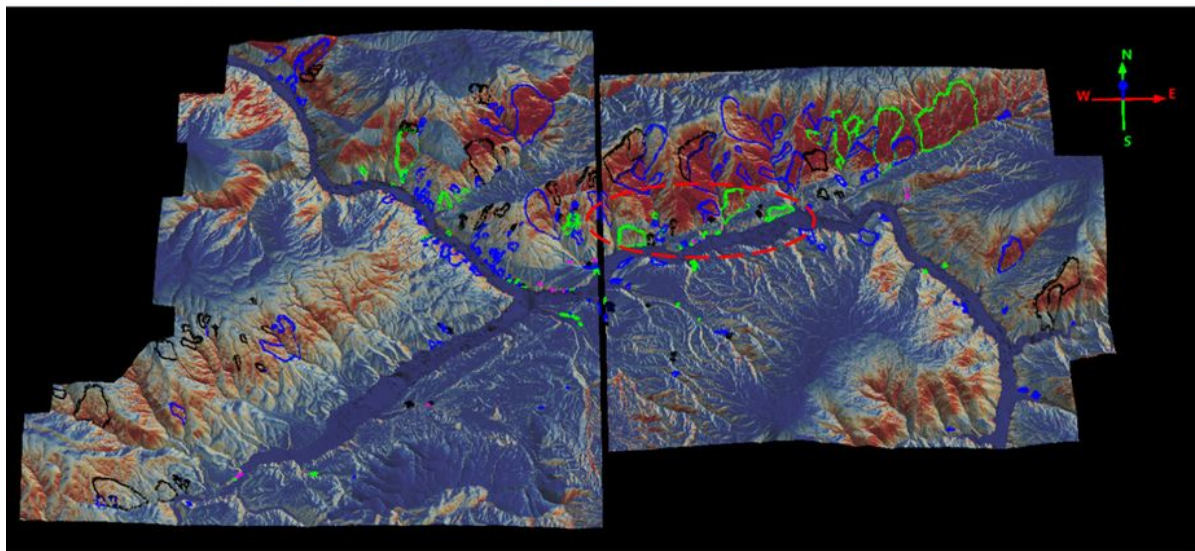


**Figure 17**

The LSMs of the study area (left: Malatya part, right: Elazig part) produced with the (a) RF and (b) MLP methods.



(a)



(b)

**Figure 18**

3D perspective views of LSMs predicted with (a) the RF and (b) the MLP algorithms together with the landslide inventory and the DSMs. The red dashed ellipses denote the area with lithological unit of unconsolidated gravel, sand, slit, clay type.

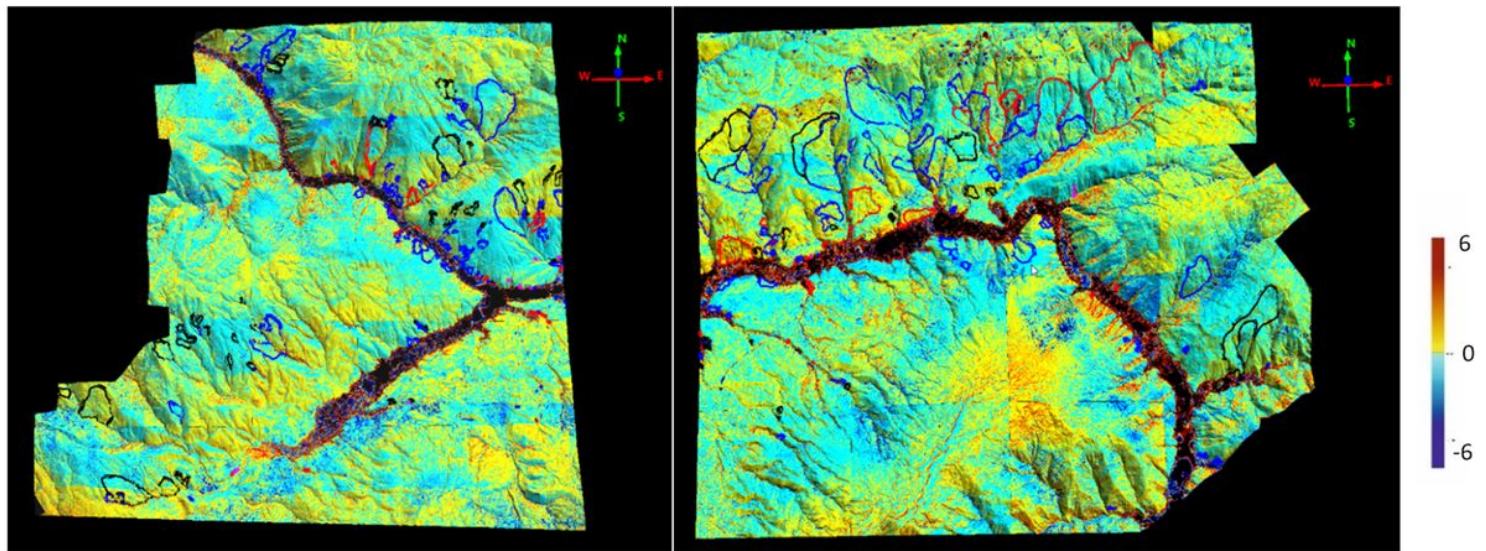


**Figure 19**

The Euclidean distance residual plots of Malatya (left) and Elazig (right) parts.

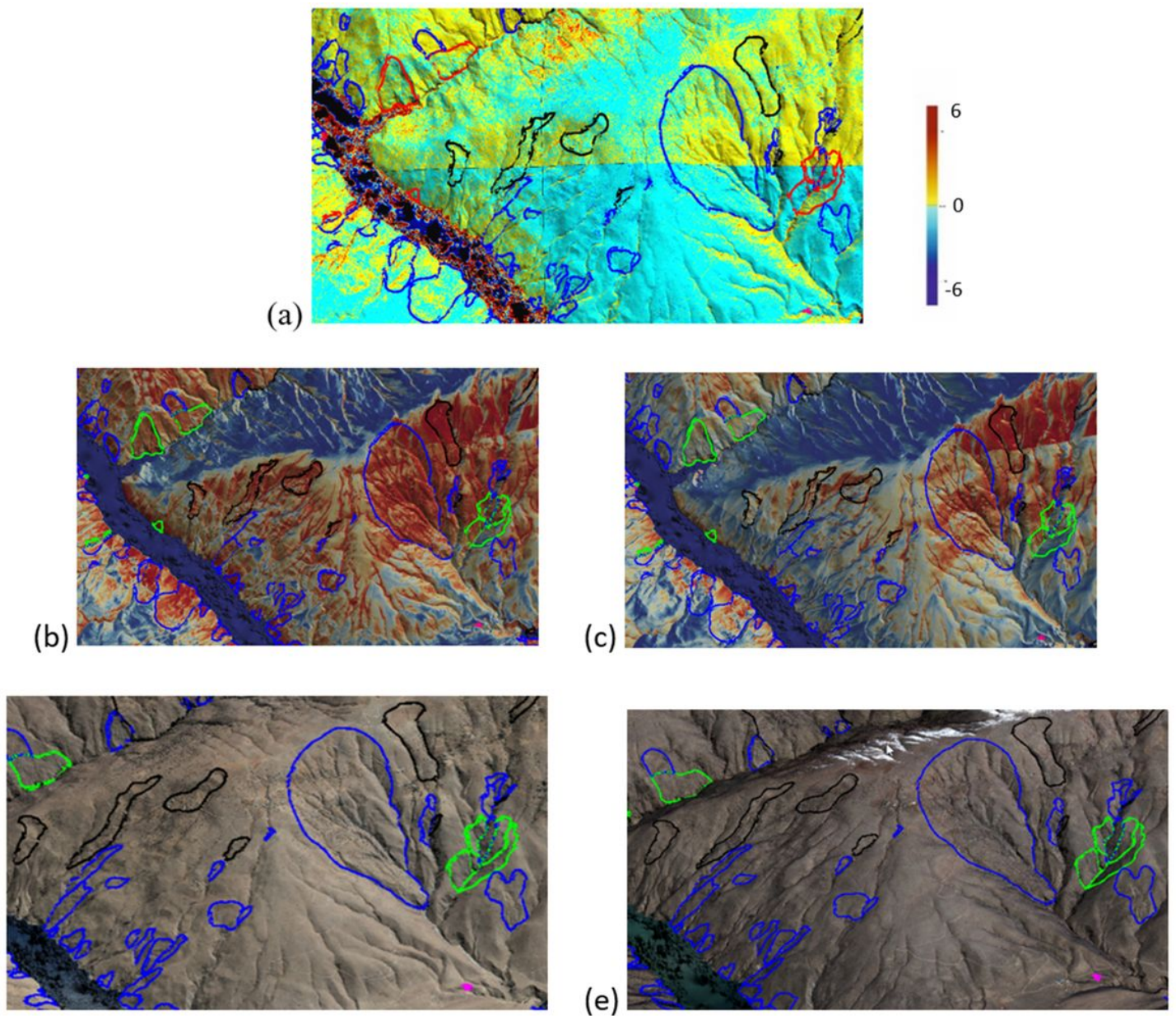


**Figure 20**

The plots of (a) the Euclidean residuals in Malatya part; (b) RF LSM; (c) MLP LSM; (d) pre-event ortophoto from 2017; and (e) post-event orthophoto from 2020; all draped on the DSMs.

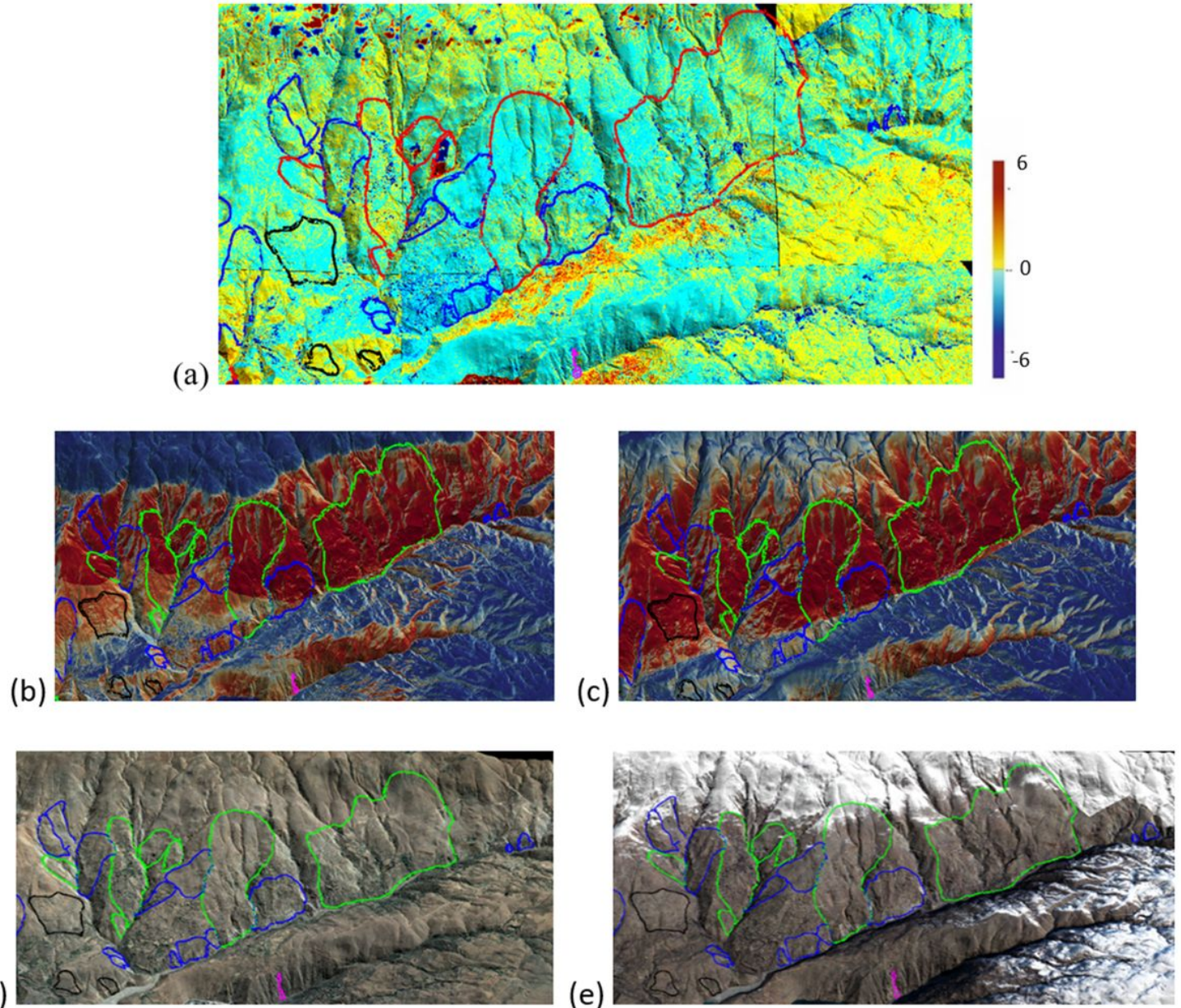


**Figure 21**

The plots of (a) the Euclidean residuals in Elazig part; (b) RF LSM; (c) MLP LSM; (d) pre-event orthophoto from 2017; and (e) post-event orthophoto from 2020; all draped on the DSMs.

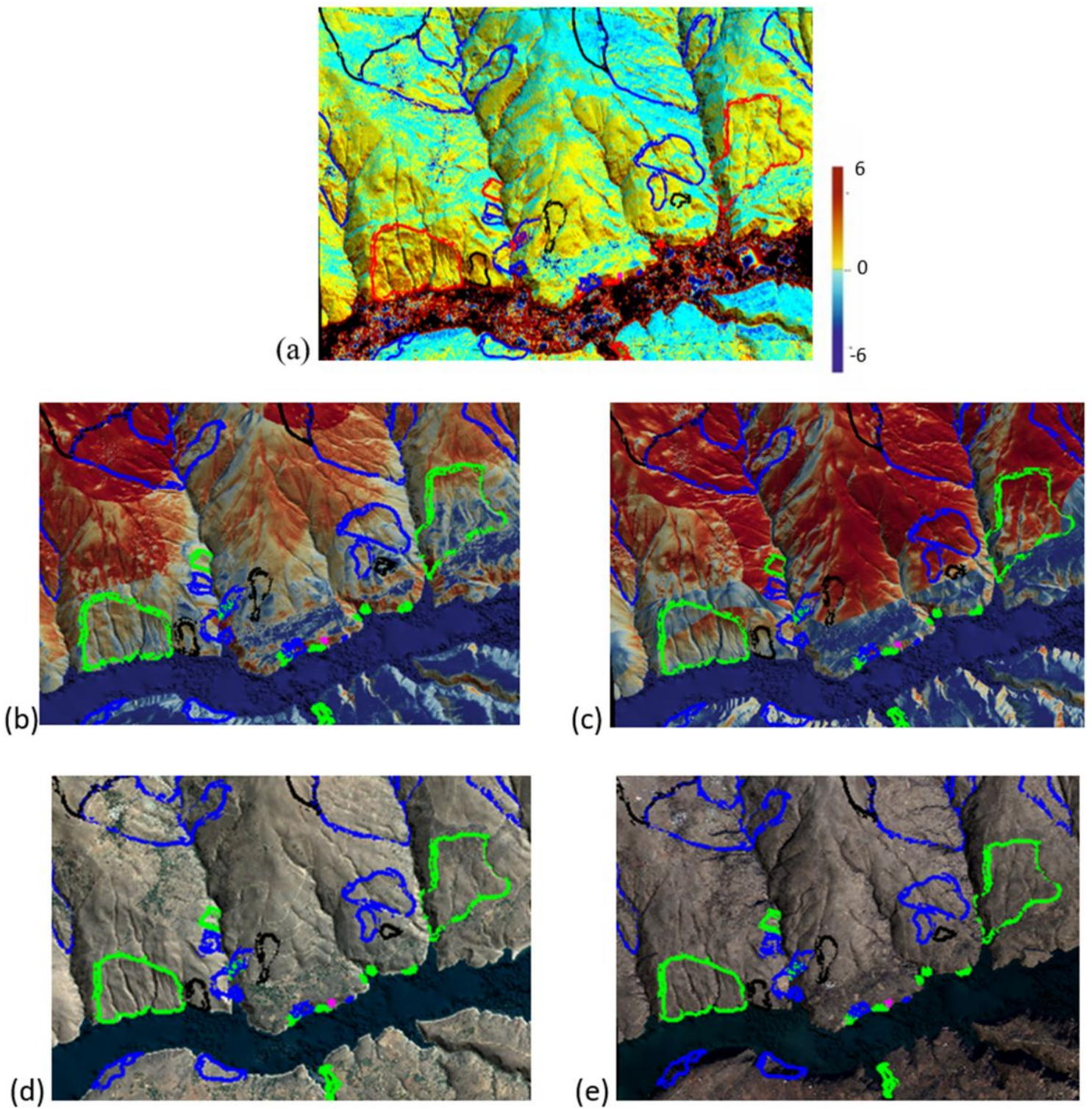


**Figure 22**

The plots of (a) the Euclidean differences in Elazig part; (b) RF LSM; (c) MLP LSM; (d) pre-event orthophoto from 2017; and (e) post-event orthophoto from 2020; draped on the DSMs. The area was selected based on the red dashed ellipses, which denote the part with lithological unit of unconsolidated gravel, sand, slit, clay type, given in Figure 18.